Thermocapillary thin-film flows on a compliant substrate

Youchuang Chao
Department of Mechanical Engineering, The University of Hong Kong, Pokfulam Road, Hong Kong, China and Department of Mechanical and Aerospace Engineering, Princeton University, Princeton, New Jersey 08544, USA

Zijing Ding*
Department of Applied Mathematics and Theoretical Physics, University of Cambridge, Wilberforce Road, Cambridge CB3 0WA, United Kingdom

(Received 11 January 2019; published 2 April 2019)

We study the dynamics of a thin liquid film on a compliant substrate in the presence of thermocapillary effect. A set of long-wave equations are derived to investigate the effects of fluid gravity (G), fluid inertia (Re), and Marangoni stresses (Ma) on the dynamics of the liquid film and the compliant substrate. By performing linear stability analysis and time-dependent computations of the long-wave equations, we examine two different cases: thin-film flows on a horizontally compliant substrate ($\beta = 0$, where β is the inclined angle) and down a vertically compliant substrate ($\beta = \pi/2$), respectively. For $\beta = 0$, we neglect fluid inertia and identify two different modes: (1) sinuous mode, where the deformations of liquid-air and liquid-substrate interfaces are in phase, which is induced by the fluid gravity, and (2) varicose mode, where the deformations of two interfaces are in phase opposition, which is induced by the Marangoni stresses. For $\beta = \pi/2$, we consider a weak fluid inertia and only observe the varicose mode driven by fluid inertia and Marangoni stresses. However, because the gravity direction is parallel to the substrate, the fluid gravity modifies the varicose mode, making the deformations of two interfaces out of phase. In particular, we also seek the nonlinear traveling-wave solutions in the case of $\beta = \pi/2$, revealing that fluid inertia and/or heating effect enhance the height and speed of the traveling waves. In both cases, the introduction of a strong wall heating gives rise to large deformations of both the thin liquid film and the compliant substrate.

DOI: 10.1103/PhysRevE.99.043101

I. INTRODUCTION

Thin-film flows on solid substrates occur widely in engineering and natural systems, such as flow-coating processes in industrial environments [1], tear-film flows in biophysical scenarios [2], as well as lava flows and gravity currents in geophysical settings [3,4]. The liquid film coating a solid substrate can be driven by gravity, surface tension, and thermo- or solutocapillary force, which received intensive attention because of their broad applications in heat and/or mass transport processes, for instance, the heat exchangers, film condensers and evaporators, and film reactors [5]. Experimental studies have demonstrated that rich dynamics are present in such systems, for instance, the development of different wave regimes [6], the occurrence of flow separation in the capillary wave region [7], the breakdown of two-dimensional (2D) wave trains into three-dimensional wave patterns [8,9], and the formation of bound states due to the interaction of solitary waves in forced film flows [10,11]. To understand these nonlinear dynamical phenomena without resorting to the direct numerical simulations of Navier-Stokes equations, various reduced-order models have been developed. For instance, the lubrication model [12,13] and Benny-type model [14,15] are used to study such kind of creeping flows, which are valid at small Reynolds numbers; the integral-boundary-layer model [16,17] and the weighted-residual integral-boundary-layer model [18,19] are employed for thin-film flows at moderate Reynolds numbers.

However, most of previous studies focus on the thin-film flows over rigid substrates, and few of them pay attention to the case of thin-film flows over compliant substrates, where the dynamics of liquid film is closely coupled with the deformation of substrate. Actually, the interactions between fluids and compliant materials are present in many situations and have been widely studied [20], such as exploring the intrusion of magma under the Earth's crust [21], liquid drops deposited on a flexible fiber array [22], deformation of elastic substrates via three-phase contact line [23], suppression of the fingering instability using an elastic membrane [24], wrinkling of thin sheet at fluid interfaces [25], and wrapping liquid droplets with elastic sheets [26]. In the case of the interactions between thin liquid films and compliant substrates, Halpern and Grotberg proposed a consistent fluid model to account for the underlying mechanisms that might cause the airway collapse of the lungs and showed how the pulmonary surfactants affect the collapse of airway [27,28]. Matar *et al*. showed that the wall flexibility enhances the instability of the flow system, and suggested a new route to improve the interfacial heat and/or mass transport and mixing [29–32]. Recently, Howell *et al*. used the lubrication theory to study the gravity-driven thin liquid film on a flexible beam and showed how the length and

*z.ding@damtp.cam.ac.uk

stiffness of the beam determine the profile of the liquid film and the flexible beam [33,34]. Zheng *et al*. investigated the self-similar solutions in the buoyancy-driven viscous liquid films on an elastic membrane, which showed excellent agreement with the experimental results [35]. Peng *et al*. considered the dynamics of a viscoelastic liquid film falling down a flexible substrate, showing that the viscoelasticity could promote the traveling speed of solitary-like hump waves [36].

Heating thin liquid films from below introduces an additional effect, which is known as the thermocapillary effect [37,38]. In practice, such Marangoni effects in thin-film flows are very important in some nonisothermal systems such as the fiber coating in industry [5]. A considerable number of works have focused on the modeling of thin-film flows on solid substrates with Marangoni effects [39–45], and some of them also examined the interaction between the Marangoni instability and the shear instability. For instance, Ruyer-Quil *et al*. applied linear stability and nonlinear wave analysis to investigate thin-film flows down a uniformly heated substrate and to show that Marangoni instability and shear instability reinforce each other in a nontrivial manner [46,47]. Recently, Saprykin *et al*. also performed 2D and 3D computations to investigate thin liquid films on topographical substrates which are also uniformly heated, indicating that droplets are vulnerable to form in the troughs of the topographical substrate and the final morphology of droplets is determined by the competition among the Marangoni effect, an additional capillary pressure brought by the substrate curvature and intermolecular forces [48]. However, these studies only consider the case of rigid substrates, and thin-film flows on compliant substrates in nonisothermal environments, which involve both the effects of wall flexibility and Marangoni stresses, have not been explored yet, despite their wide presence in various areas. For instance, in materials engineering, the Marangoni effect is introduced to induce the formation of wrinkle patterns at the surface of soft materials [49], and in cosmetics, the nonuniform distributions of cosmetics coating on the soft skins might be also caused by the Marangoni effect [50]. Nevertheless, how the Marangoni stresses affect the dynamics of the thin liquid film and the underlying compliant substrate is still an open question.

In this paper, by applying long-wave asymptotics, elasticity theory, and Fourier's law, we introduce a coupled model to describe the dynamic response of thin-film flows over a compliant substrate with an inclined angle β in the presence of uniform heating, as shown in Fig. 1. We explore fluid gravity and fluid inertia in addition to the Marangoni effect of the liquid film to understand the behavior of this coupled system. In Sec. II, we present the mathematical model which describes the equations for the heated liquid film with those for the deflection of the compliant substrate. In Sec. III, we consider the case of a horizontal substrate ($\beta = 0$) and derive a set of lubrication-type evolution equations. The linear stability analysis and nonlinear simulations are carried out to study the effects of fluid gravity and Marangoni stresses. In Sec. IV, we further consider the case of a vertical substrate ($\beta = \pi/2$) and obtain a set of Benney-type evolution equations which involve a weak fluid inertia. In this section, apart from the linear stability analysis and nonlinear simulations, we also examine the effects of fluid inertia and Marangoni stresses on the nonlinear traveling-wave solutions. In both cases, we compare the results of nonlinear simulations with the predictions from the linear stability analysis and/or traveling-wave solutions. We draw our conclusions in Sec. V.

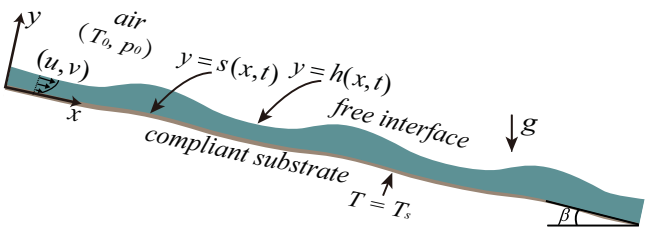

FIG. 1. Schematic of a thin liquid film on an infinitely large, heated, flexible, and impermeable substrate. x and y denote the streamwise and normal directions; u and v denote the streamwise and normal velocities, respectively. The substrate is uniformly maintained with a temperature T_s; the reference temperature and pressure in air are T_0 and p_0, respectively. The instantaneous locations of the substrate and the liquid film are denoted by $y = s(x,t)$ and $y = h(x,t)$, respectively.

II. PROBLEM DEFINITION

We study the dynamics of Newtonian liquid films flowing down a heated compliant substrate, as shown in Fig. 1. A two-dimensional Cartesian coordinate system (x, y) is employed to describe the dynamics, where x and y denote the streamwise and normal directions to the substrate, respectively. The density ρ, dynamic viscosity μ, and thermal diffusivity k of the liquid are assumed to be constant. The compliant substrate is assumed to be infinitely long, thin, impermeable, and isotropic, and the flow is heated by the substrate, which is maintained at a constant temperature T_s. We also assume that the surrounding air is passive and inviscid and neglect its dynamics. The instantaneous shape of the substrate and the height of the liquid film are denoted by $y = s(x,t)$ and $y = h(x,t)$, and the initial stationary locations of the substrate and the liquid film are $y = 0$ and $y = h_0$, respectively. Therefore, in $s(x,t) \leqslant y \leqslant h(x,t)$, the dynamics of the heated liquid flow is governed by the continuity and momentum equations, and the heat transfer is governed by the energy equation as follows:

$$\nabla \cdot \boldsymbol{u} = 0, \tag{1a}$$

$$\rho[\boldsymbol{u}_t + (\boldsymbol{u}\cdot\nabla)\boldsymbol{u}] = -\nabla p + \mu\nabla^2\boldsymbol{u} + \rho\boldsymbol{g}, \tag{1b}$$

$$T_t + (\boldsymbol{u}\cdot\nabla)T = k\nabla^2 T, \tag{1c}$$

where $\boldsymbol{u} = u\boldsymbol{e}_x + v\boldsymbol{e}_y$, p, and T represent the velocity, pressure, and temperature fields and $\boldsymbol{g}$ is the gravitational acceleration. The symbols in the subscript denote the partial derivatives with respect to the corresponding variables. Unless stated otherwise, all the subscripts represent the partial derivatives.

We assume that the compliant substrate is sufficiently thin so that its tension acts uniformly across the thickness of the substrate [51]. The thermal stresses in the substrate are negligible due to the uniform heating. In addition, the inertia of the substrate is neglected because of the slow motion of the

substrate [24,52,53]. Therefore, the balance of normal stresses on the substrate, $y = s(x,t)$, gives [52]

$$\frac{\rho_s h_s d_s}{\left(1+s_x^2\right)^{1/2}} s_t = -\sigma_s \nabla \cdot \boldsymbol{n}_s + \boldsymbol{n}_s \cdot \mathcal{T} \cdot \boldsymbol{n}_s, \tag{2}$$

where ρ_s, h_s, d_s, and σ_s are the density, thickness, damping coefficient, and tension of the substrate; $\mathcal{T} = -p\boldsymbol{I} + \mu[\nabla \boldsymbol{u} + (\nabla \boldsymbol{u})^T]$ is the Newtonian stress tensor in the liquid; $\boldsymbol{n}_s$ and $-\nabla \cdot \boldsymbol{n}_s$ are the surface norm vector and mean curvature of the substrate, respectively.

In fact, Eq. (2) is a simplified forced membrane equation, which couples the restoring force of the substrate with the normal force imposed by the outer fluid, and this force balance neglects the bending stresses. This model has been widely applied to investigate the dynamics of liquid films inside flexible tubes [27,28,54], as well as the stability of thin-film flows on flexible inclines [29–32,36].

On the surface of the substrate, $y = s(x,t)$, we apply the no-slip boundary condition

$$u = 0. \tag{3a}$$

The kinematic condition on the surface of the substrate, $y = s(x,t)$, is written as

$$v = s_t + u s_x. \tag{3b}$$

On the free surface of liquid, $y = h(x,t)$, the stress balance is written as

$$\mathcal{T} \cdot \boldsymbol{n}_i = \nabla_s \sigma - \sigma(\nabla_s \cdot \boldsymbol{n}_i)\boldsymbol{n}_i, \tag{3c}$$

where $\boldsymbol{n}_i$ and $\boldsymbol{t}_i$ denote the unit normal and unit tangential vectors of the free liquid interface, respectively. ∇_s and $-\nabla_s \cdot \boldsymbol{n}_i$ are the surface gradient operator and the mean curvature of the free liquid surface, respectively.

The temperature on the substrate, $y = s(x,t)$, is imposed as

$$T = T_s. \tag{3d}$$

On the free liquid interface, $y = h(x,t)$, the heat balance is governed by the Newton's law of cooling,

$$-\lambda \nabla T \cdot \boldsymbol{n_i} = h_g(T - T_\infty), \tag{3e}$$

where λ and h_g are the thermal conductivity and the heat transfer coefficient of the liquid, respectively. T_∞ is the ambient temperature far away from the free liquid interface and is chosen as the reference temperature T_0.

On the free liquid interface, $y = h(x,t)$, the kinematic condition is given as

$$v = h_t + u h_x, \tag{3f}$$

where we assume the liquid is nonvolatile and the evaporation is neglected.

To model the Marangoni effect on the free liquid interface, $y = h(x,t)$, we assume a linear constitutive relation for the surface tension σ, given by

$$\sigma = \sigma_0 - \sigma_T(T^i - T_0), \tag{4}$$

where σ_T is the surface tension constant, σ_0 is the surface tension at reference temperature T_0, and T^i is the temperature at the free liquid interface. For most liquids, σ_T is positive, where their surface tensions decrease monotonically with increasing the temperature [43,55].

III. LIQUID FILM FLOWS ON A HORIZONTAL SUBSTRATE: $\beta = 0$

We first consider a horizontal substrate where $\beta = 0$ and assume Re $\ll O(1)$. Therefore, the lubrication theory is applied to derive the evolution equations.

A. Scaling and asymptotic modeling

By scaling, we could eliminate all of the physical variables from the differential equations and then obtain the dimensionless governing system. We introduce the typical wavelength $\mathscr{L}$ and the mean thickness of the liquid film h_0 as the length scales in the x and y directions, respectively. In addition, a small long-wave parameter $\epsilon = h_0/\mathscr{L} = O(10^{-1})$ is introduced into the system. Therefore, we adopt the following nondimensional variables, denoted by asterisks [13],

$$\begin{aligned} &(x,y) = \mathscr{L}(x^*, \epsilon y^*), \quad (u,v) = \mathscr{U}(u^*, \epsilon v^*), \\ &(h,s) = h_0(H^*, S^*), \quad t = \frac{\mathscr{L}}{\mathscr{U}} t^*, \\ &p - p_a = \frac{\mu \mathscr{U} \mathscr{L}}{h_0^2} p^*, \quad T - T_\infty = (T_s - T_\infty) T^*, \end{aligned} \tag{5}$$

where the velocity scale, $\mathscr{U} = \mu/\rho h_0$, given by the balance between inertia and viscous drag.

After rescaling the dimensional governing Eqs. (1a)–(1c) and dropping all $*$ superscripts from the variables for notational clarity, we obtain the leading-order dimensionless governing equations,

$$u_x + v_y = 0, \tag{6a}$$

$$-p_x + u_{yy} + \epsilon^{-1} G \sin\beta = 0, \tag{6b}$$

$$p_y + G\cos\beta = 0, \tag{6c}$$

$$T_{yy} = 0, \tag{6d}$$

where $G = \rho g h_0^3/\mu \mathscr{U} \mathscr{L}$ is the gravity number.

On the surface of the substrate, $y = S(x,t)$, the boundary conditions at the leading order yield

$$u = 0, \quad S_t = v, \quad T = 1. \tag{7}$$

The leading-order stress balance on the substrate, $y = S(x,t)$, can be written as

$$B_s S_t = W_s S_{xx} + p_w - p, \tag{8}$$

where $B_s = \rho_s h_s d_s h_0^3/\mu \mathscr{L}^2$ is a dimensionless damping number and $W_s = \sigma_s h_0^3/\mu \mathscr{U} \mathscr{L}^3$ is the dimensionless tension coefficient, where smaller values of B_s and/or W_s indicate that the substrate is more flexible and larger values of B_s and/or W_s indicate that the substrate is more rigid [27]. On the free liquid interface, $y = H(x,t)$, the leading-order boundary conditions are reduced as

$$u_y + \mathrm{Ma} T_x^i = 0, \quad p + \mathrm{We} H_{xx} = 0, \quad T_y + \mathrm{Bi} T = 0, \tag{9}$$

where $\mathrm{Ma} = \sigma_T h_0 (T_s - T_\infty)/\mu \mathscr{U} \mathscr{L}$ is the Marangoni number, $\mathrm{We} = \sigma_0 h_0^3/\mu \mathscr{U} \mathscr{L}^3$ is the Weber number, and $\mathrm{Bi} = h_g h_0/\lambda$ is the Biot number.

The dimensionless kinematic condition at the free liquid interface, $y = H(x,t)$, is given as

$$v = H_t + uH_x. \tag{10}$$

After solving the corresponding leading-order equations, we obtain the distributions of leading-order velocity and pressure fields, u and p, given by

$$u = \tfrac{1}{2}(p_x - \epsilon^{-1}G\sin\beta)y^2 + b_1 y + b_2, \tag{11a}$$

where

$$p = -G\cos\beta(y - H) - \mathrm{We}H_{xx}, \tag{11b}$$

$$b_1 = -p_x H + \frac{\mathrm{MaBi}}{[1 + \mathrm{Bi}(H - S)]^2}(H - S)_x, \tag{11c}$$

$$b_2 = -\frac{1}{2}p_x S^2 - b_1 S. \tag{11d}$$

The leading-order solution of the temperature distribution is

$$T = 1 - \frac{\mathrm{Bi}(y - S)}{1 + \mathrm{Bi}(H - S)}, \tag{12a}$$

where the temperature at free liquid interface, $y = H(x,t)$, is given as

$$T^i = \frac{1}{1 + \mathrm{Bi}(H - S)}. \tag{12b}$$

After substituting Eq. (11a) into the Eq. (10) which is in the form of mass conservation

$$(H - S)_t + \partial_x \int_S^H u dy = 0. \tag{13}$$

We eventually obtain the evolution equations of (H, S), given by

$$(H - S)_t + \left[\tfrac{1}{6}(p_x - \epsilon^{-1}G\sin\beta)(H^3 - S^3) + \tfrac{1}{2}b_1(H^2 - S^2) + b_2(H - S)\right]_x = 0, \tag{14a}$$

$$B_s S_t - W_s S_{xx} - \mathrm{We}H_{xx} - G\cos\beta(1 - H + S) = 0. \tag{14b}$$

The solutions of Eqs. (14a) and (14b), $H(x,t)$ and $S(x,t)$, describe the instantaneous shape of the air-liquid interface and the instantaneous deformation of the compliant substrate, respectively. In this section, we only consider the case of a horizontal substrate ($\beta = 0$), and therefore, the gravity term in the horizontal direction ($\epsilon^{-1}G\sin\beta$) could be removed from Eq. (14a), and the gravity term in the vertical direction ($G\cos\beta$) becomes G in Eq. (14b), respectively. By setting $S = 0$, we could recover the lubrication-type equation derived by Oron [56], who studied the dynamics of thin liquid films on a heated solid substrate. In this section, we mainly focus on the effects of fluid gravity (G) and Marangoni stresses (Ma) on the dynamics of the liquid film and substrate, and therefore, in most situations, we fix the Biot number (Bi), Weber number (We), wall damping (B_s), and wall tension (W_s) as 1, 10, 1, and 10, respectively. The typical nondimensional numbers used in this paper are from previous work by Halpern *et al*. [27,28] and Kalliadasis *et al*. [5].

B. Linear stability analysis

To begin with, we investigate the features characterizing the onset of instability via the linear stability analysis. With a constant thickness of the film, no deformation of the compliant substrate, and no flow, the evolution Eqs. (14a) and (14b) admit a uniform solution,

$$\bar{H} = 1, \quad \bar{S} = 0. \tag{15}$$

To this end, Eqs. (14a) and (14b) are perturbed around the above base state by posing the expansion

$$[H, S] = [\bar{H}, \bar{S}] + [H', S']. \tag{16}$$

Therefore, we yield

$$(H' - S')_t - \frac{G}{3}H'_{xx} + \frac{\mathrm{We}}{3}H'_{xxxx} + \frac{\mathrm{MaBi}}{2(1 + \mathrm{Bi})^2}(H' - S')_{xx} = 0, \tag{17a}$$

$$B_s S'_t - W_s S'_{xx} - \mathrm{We}H'_{xx} - G(-H' + S') = 0. \tag{17b}$$

Following a standard approach, we apply a normal mode analysis, expressed by

$$[H', S'] = [\hat{H}, \hat{S}]\exp(ikx + \omega t), \tag{18}$$

where $[\hat{H}, \hat{S}]$ are the Fourier amplitudes of the disturbances, $\omega = \omega_r + i\omega_i$ is the complex frequency, and k is the wave number, respectively. The real part ω_r and imaginary part ω_i represent the effective growth rate and frequency of the linear instability disturbance, respectively. Finally, by substituting Eq. (18) into Eqs. (17a) and (17b), we obtain the dispersion relation

$$\omega\begin{pmatrix}\hat{H}\\ \hat{S}\end{pmatrix} = \begin{pmatrix}\mathcal{L}_{11} & \mathcal{L}_{12}\\ \mathcal{L}_{21} & \mathcal{L}_{22}\end{pmatrix}\begin{pmatrix}\hat{H}\\ \hat{S}\end{pmatrix}, \tag{19a}$$

where

$$\mathcal{L}_{11} = -\frac{\mathrm{We}k^2 + G}{B_s} - \frac{\mathrm{We}k^4 + Gk^2}{3} + \frac{\mathrm{MaBi}k^2}{2(1 + \mathrm{Bi})^2}, \tag{19b}$$

$$\mathcal{L}_{12} = \frac{-W_s k^2 + G}{B_s} - \frac{\mathrm{MaBi}k^2}{2(1 + \mathrm{Bi})^2}, \tag{19c}$$

$$\mathcal{L}_{21} = -\frac{\mathrm{We}k^2 + G}{B_s}, \tag{19d}$$

$$\mathcal{L}_{22} = \frac{-W_s k^2 + G}{B_s}. \tag{19e}$$

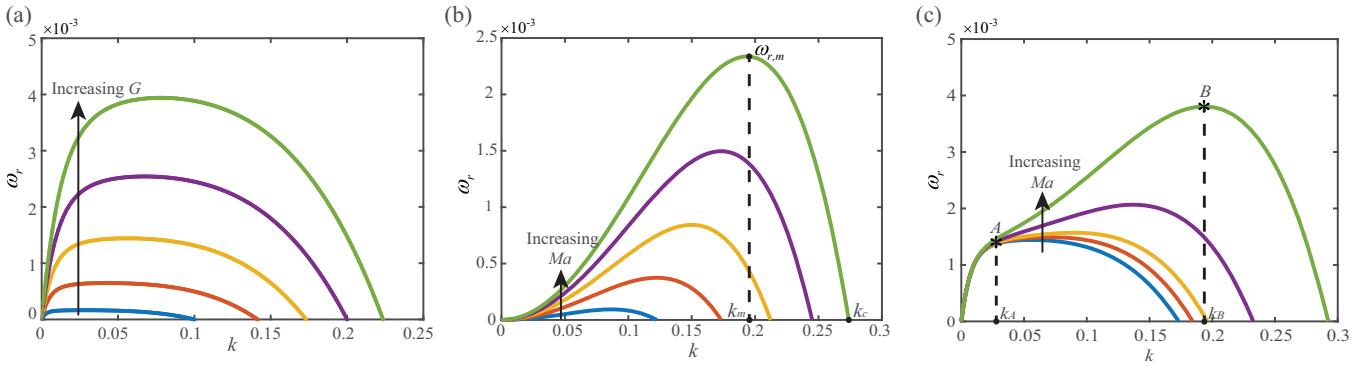

FIG. 2. The dispersion curves $\omega_r(k)$ showing the effects of (a) fluid gravity ($G = 0.1, 0.2, 0.3, 0.4, 0.5$) without Maranogni stresses (Ma = 0); (b) Marangoni stresses (Ma = 0.2, 0.4, 0.6, 0.8, 1) without fluid gravity ($G = 0$); (c) Marangoni stresses (Ma = 0, 0.1, 0.2, 0.5, 1) with fluid gravity ($G = 0.3$). The k_m, $\omega_{r,m}$, and k_c labeled in (b) denote the most dangerous wave number, maximal effective growth rate, and cut-off wave number, respectively. Other parameters: We = 10, $B_s = 1$, $W_s = 10$, $\beta = 0$, and Bi = 1.

By requiring the matrix in Eq. (19a) to be singular, we could obtain the dispersion curves $\omega_r(k)$ which show the effects of the gravity number (G) and Marangoni number (Ma) on the linear stability, as shown in Figs. 2(a) and 2(b), respectively. These dispersion curves clearly illustrate the most dangerous mode, k_m, and their associated maximal effective growth rate, $\omega_{r,m}$, as well as the cutoff mode, k_c. We observe that increasing G and/or Ma result in the increase of the maximal effective growth rate ($\omega_{r,m}$) and a shift of wave numbers that associated with the maximal effective growth rate(k_m) and cutoff wave numbers (k_c) into larger values [see Figs. 2(a) and 2(b)]. However, compared with the case of thin liquid films without any heating effects (Ma = 0), introduction of a relatively strong heating effect (Ma = 1) makes the most unstable wave number k_m that corresponds to the largest growth rate $\omega_{r,m}$ shift into larger values, indicating that the instability is taken over by Marangoni effect, as shown in Fig. 2(c). Therefore, by introducing the Marangoni stresses, we expect a shift from an instability characterized with a long wavelength [see point A in Fig. 2(c)] into that characterized with a relatively short wavelength [see point B in Fig. 2(c)]. To account for this observation, we consider the case of a rigid substrate and the dispersion relationship becomes $\omega_r = k^2[-\frac{G}{3} - \frac{\mathrm{We}}{3}k^2 + \frac{\mathrm{MaBi}}{2(1+\mathrm{Bi})^2}]$, where the most unstable mode and the cutoff mode are obtained as $k_m = \sqrt{-\frac{G}{2\mathrm{We}} + \frac{3\mathrm{MaBi}}{4\mathrm{We}(1+\mathrm{Bi})^2}}$ and $k_c = \sqrt{-\frac{G}{\mathrm{We}} + \frac{3\mathrm{MaBi}}{2\mathrm{We}(1+\mathrm{Bi})^2}}$, respectively. We find that the corresponding most unstable wavelength ($2\pi/k_m$) and cut-off wavelength ($2\pi/k_c$) decrease with increasing the values of Ma, which indicates that the long-wave thermocapillary instabilities could shift into instabilities with relatively short wavelengths when a very strong Marangoni effect is present. These results will be verified later by the time-dependent simulations of the long-wave evolution Eqs. (14a) and (14b).

To have a clear view of the two destabilizing effects, we further obtain the neutral stability curves in the k_c-Ma plane with varying G. The cutoff wave number k_c is calculated by setting $\omega_r = 0$ to be zero, given as

$$\mathcal{L}_{11}\mathcal{L}_{22} - \mathcal{L}_{12}\mathcal{L}_{21} = 0. \tag{20}$$

We notice that when the values of Ma are very small (Ma $<$ 1), the unstable regimes expand significantly with increasing G; however, as we increase Ma into large values (Ma $>$ 1), the unstable regimes expand significantly with increasing Ma rather than G (see Fig. 3). Therefore, according to these observations, we hypothesize that two different regimes might be present, which are mainly dominated by gravitational force and Marangoni force, respectively.

C. Nonlinear simulations

To verify our hypothesis and further identify how the fluid gravity and Marangoni stresses affect the spatiotemporal profiles of the liquid film and substrate, we must consider the full nonlinear evolution equations. The problem is further reduced by assuming that the liquid film and the substrate are large enough, and thus periodic boundary conditions could be applied in a defined finite domain, $x \in [0, L]$. The spatial solutions of Eqs. (14a) and (14b) are approximated by the

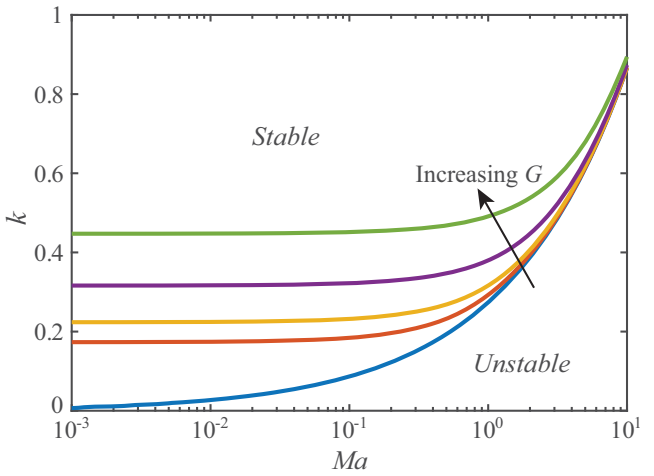

FIG. 3. Neutral stability curves in the parameter space spanned by Ma-k for $G = 0, 0.3, 0.5, 1$, and 2. Other parameters: We = 10, $B_s = 1$, $W_s = 10$, $\beta = 0$, and Bi = 1.

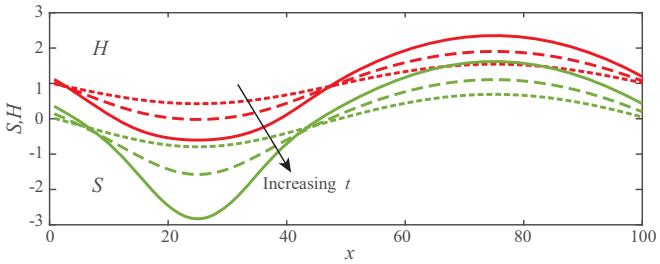

FIG. 4. The profiles of liquid film H [upper (red) lines] and substrate S [lower (green) lines] at $t = 400, 800, 1200$ with $G = 0.3$ and $\mathrm{Ma} = 0$. Other parameters: $\mathrm{We} = 10$, $B_s = 1$, $W_s = 10$, $\beta = 0$, $\mathrm{Bi} = 1$, and $L = 100$.

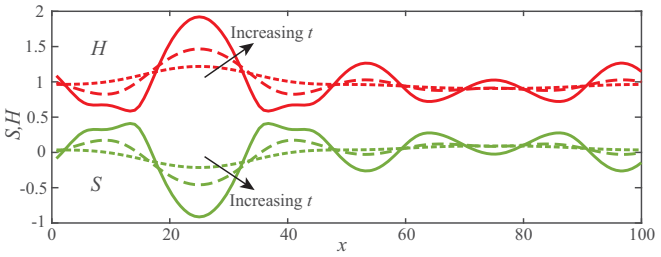

FIG. 5. The profiles of liquid film H [upper (red) lines] and substrate S [lower (green) lines] at $t = 900, 1100, 1250$ with $\mathrm{Ma} = 2$ and $G = 0$. Other parameters: $\mathrm{We} = 10$, $B_s = 1$, $W_s = 10$, $\beta = 0$, $\mathrm{Bi} = 1$, and $L = 100$.

discrete Fourier series, in the form of

$$H(x,t) = \sum_{-N/2}^{N/2} \hat{H}_n(t)\exp(2in\pi x/L), \tag{21a}$$

$$S(x,t) = \sum_{-N/2}^{N/2} \hat{S}_n(t)\exp(2in\pi x/L), \tag{21b}$$

where $\hat{H}_n(t)$ and $\hat{S}_n(t)$ are the Fourier coefficients and N is the Fourier mode. In this paper, we use 256 Fourier modes which guarantee sufficient accuracy of solutions.

At initial time $t = 0$, a harmonic perturbation is imposed on the free liquid interface $H(x)$ and the compliant substrate $S(x)$ remains flat, given by

$$H(x,0) = 1 + 0.1\sin(2\pi x/L), \tag{22a}$$

$$S(x,0) = 0. \tag{22b}$$

The resulting system, consisting of the ordinary differential equations (ODEs) and the periodic boundary constraints, is solved by an implicit Gear's method in time with a relative error less than 10^{-6} [57].

We observe two different regimes due to the presence of gravity and wall heating, respectively, which is in consistent with the predictions by the linear stability analysis. Typical results showing the effect of the gravity ($G = 0.3$) on the profiles of the liquid film and the compliant substrate without any heating ($\mathrm{Ma} = 0$) at $t = 400,\ 800$, and 1200 are illustrated in Fig. 4. We notice that when the Marangoni effect is absent ($\mathrm{Ma} = 0$), the deformation direction of substrate is the same as that of the liquid film, which is caused by the fluid gravity and the mode is termed as *sinuous mode*. However, with the introduction of the heating effect ($\mathrm{Ma} = 2$) and neglecting the gravity ($G = 0$), a totally different phenomenon is present. As the time increases, we observe that the deformation of the substrate is in the opposite direction as that of the liquid film, which is caused by the Marangoni stresses and this new mode is termed the *varicose mode* (see Fig. 5). The characteristic length of patterns induced by Marangoni stresses is smaller than that induced by fluid gravity, indicating that the most unstable wave number of Marangoni-driven flows is larger than the case of gravity-driven flows, agreeing well with the predications from linear stability analysis.

Compared with the case of a mild heating ($\mathrm{Ma} = 0.5$), a very strong heating ($\mathrm{Ma} = 5$) on the liquid film gives rise to the emergence of secondary and even higher-order patterns surrounding the main patterns, as shown in Figs. 6(a) and 6(b). The physical mechanism of the Marangoni effect can be explained by assuming that a liquid film is initially depressed at a certain region due to a randomly external perturbation. When this film is heated, this depressed region has a lower surface tension compared with that of its neighbors. Afterward, Marangoni stresses, induced by the surface tension gradients, are generated and drive liquids from this hot region toward its neighboring cold regions, accelerating instability of the system [58]. Finally, due to the Marangoni stresses, the liquids gradually accumulate into the cold regions, which results in the increase of liquid mass in these local cold regions and thus exacerbates the deformation of the compliant substrate. Therefore, the deformation of the liquid films induced by the Marangoni stresses further leads to the opposite deformation of the compliant substrate.

When both the gravity and Marangoni effect are present, where $G = 0.3$ and $\mathrm{Ma} = 2$, we could observe the interaction between the sinuous and varicose modes where a *mixed mode* is present, as shown in Figs. 7(a)–7(d). In this case, at an early stage, $t < 300$, the instability is dominated by gravity and the main mode is sinuous mode [Figs. 7(a) and 7(b)]. However, at a later stage, $t > 550$, the instability is taken over by varicose mode, where the Marangoni effect starts playing an important role and even smaller patterns emerge on the basis of sinuous mode [Figs. 7(c) and 7(d)].

In addition, when we increase the wall damping and wall tension coefficients from small values, where $B_s = 1$ and $W_s = 10$, into very large values, where $B_s = 10^3$ and $W_s = 10^4$, we observe that the compliant substrate recovers as a rigid substrate [see Figs. 8(a), 8(b), 9(a), and 9(b)]. Physically, the wall damping and wall tension from the compliant substrate are to dissipate the kinetic energy, and therefore larger values of wall damping and wall tension have stronger dissipation ability and make the system more stable. Here we first consider the effects of fluid gravity ($G = 0.3, \mathrm{Ma} = 0$): For the case of a very rigid substrate ($B_s = 10^3$, $W_s = 10^4$), the initial perturbation in form of Eq. (22) gradually damps and the liquid-air interface eventually becomes flat, which is because of the stabilizing effects of fluid gravity and wall rigidity, as shown in Fig. 8(b). In contrast, for the case of a very compliant substrate ($B_s = 1$, $W_s = 10$), due to the wall

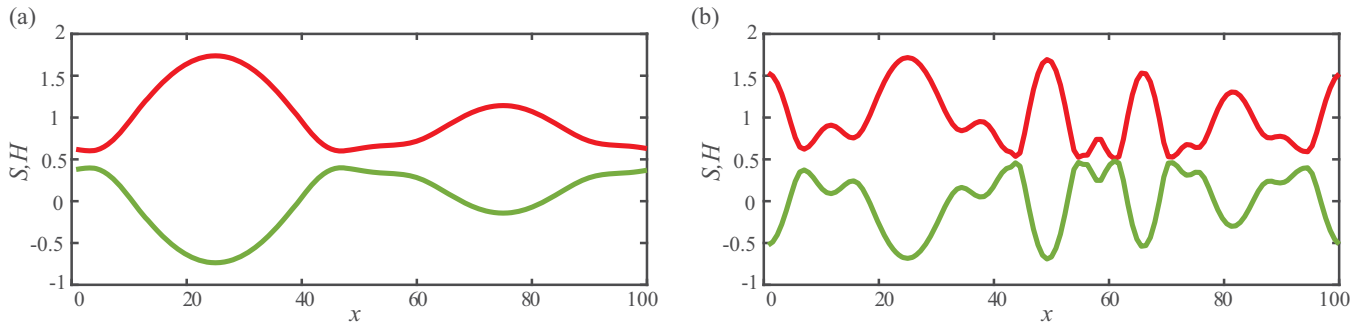

FIG. 6. The profiles of liquid film H [upper (red) line] and substrate S [lower (green) line] with (a) Ma $= 0.5$, $G = 0$ at $t = 9000$; (b) Ma $= 5$, $G = 0$ at $t = 370$. Other parameters: We $= 10$, $B_s = 1$, $W_s = 10$, $\beta = 0$, Bi $= 1$, and $L = 100$.

flexibility, the fluid gravity plays a destabilizing role where both the liquid-air and liquid-substrate interfaces deform in the same direction, as shown in Fig. 8(a). However, if we only consider the effects of wall heating ($G = 0$, Ma $= 2$), for the case of a very compliant substrate ($B_s = 1$, $W_s = 10$), the synergistic effect between wall flexibility and wall heating gives rise to the opposite deformations of liquid-air and liquid-substrate interfaces, in contrast to results of the case of a very rigid substrate ($B_s = 10^3$, $W_s = 10^4$), as shown in Figs. 9(a) and 9(b), respectively.

Moreover, the length of computational domain (L) also has significant effects on the time-dependent numerical results [56]. Below a critical computational length, we could not observe any instabilities (see Appendix B for detailed discussions), indicating that thermocapillary instabilities with short wavelengths are suppressed, which agrees well with the predications from linear stability analysis. Therefore, in this section, based on the deformation directions of the liquid-air and liquid-substrate interfaces, we observe two different modes including sinuous and varicose modes, which are caused by the fluid gravity and Marangoni effect, respectively.

IV. LIQUID FILM FLOWS DOWN A VERTICAL SUBSTRATE: $\beta = \pi/2$

We now turn to the case of thin-film flows down a vertical substrate ($\beta = \pi/2$) with a small Reynolds number (Re $\simeq 1$) and reconstruct the nonlinear evolution equations.

A. Scaling and asymptotic modeling

In this section, we introduce a new scaling, as follows [5]:

$$
\begin{aligned}
&(x, y, h, s) = h_0(x^*, y^*, H^*, S^*),\\
&(u, v) = \frac{h_0^2}{t_v l_v}(u^*, v^*), \quad t = \frac{t_v l_v}{h_0} t^*, \\
&p - p_g = \frac{\rho l_v h_0}{t_v^2} p^*, \quad T - T_\infty = (T_s - T_\infty) T^*.
\end{aligned}
\tag{23}
$$

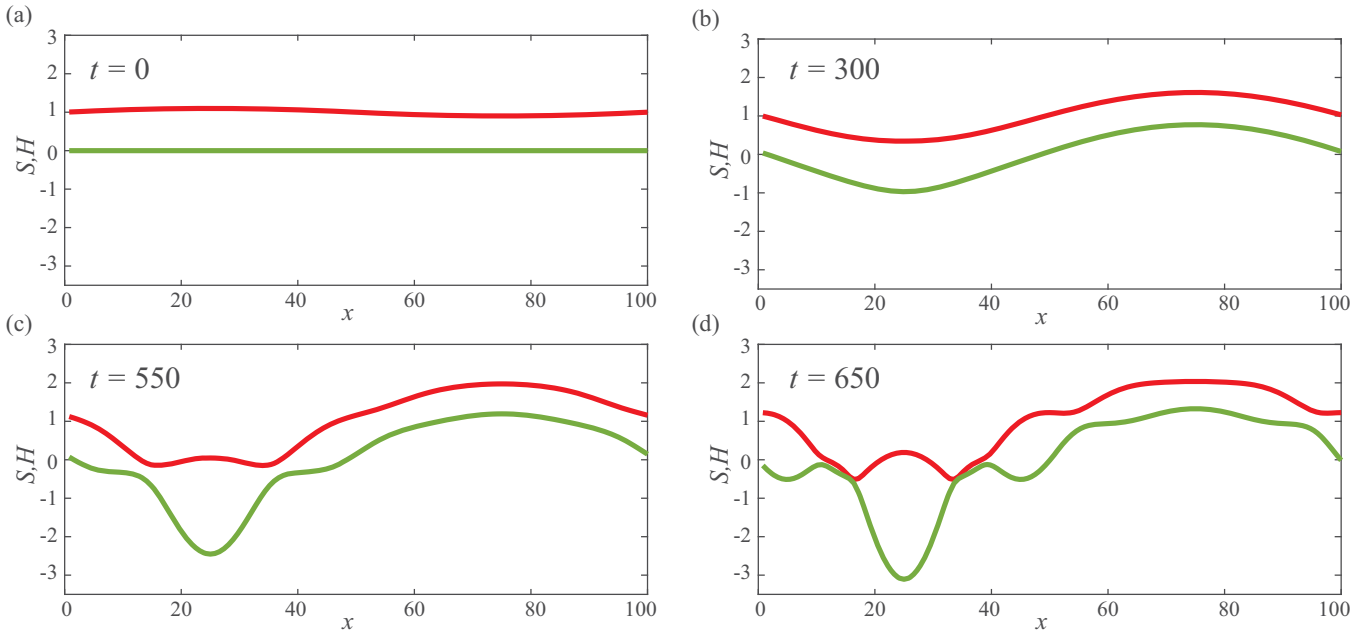

FIG. 7. The profiles of liquid film H [upper (red) lines] and substrate S [lower (green) lines] with $G = 0.3$, Ma $= 2$ at $t = 0,\ 300,\ 550,$ and 650. Other parameters: We $= 10$, $B_s = 1$, $W_s = 10$, $\beta = 0$, Bi $= 1$, and $L = 100$.

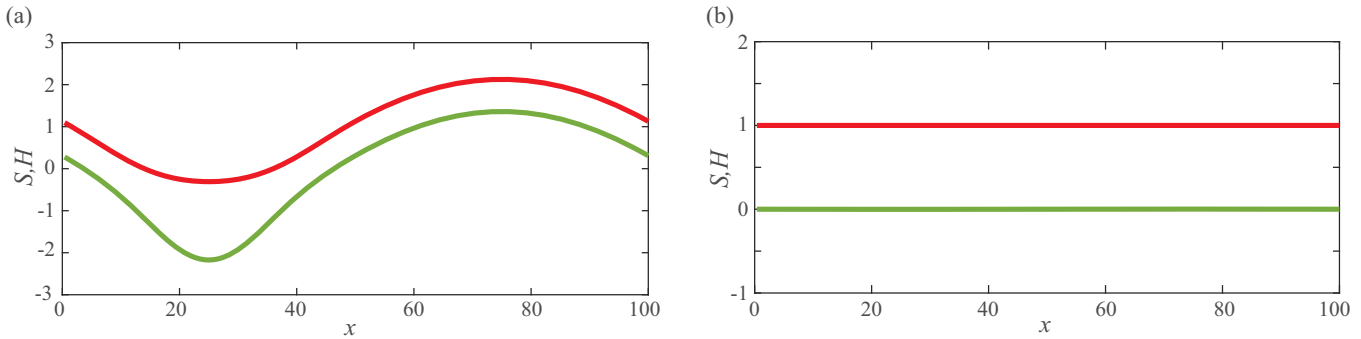

FIG. 8. The profiles of liquid film H [upper (red) line] and substrate S [lower (green) line] for (a) the case of a very compliant substrate with $B_s = 1, W_s = 10$ at $t = 1000$; (b) the case of a very rigid substrate with $B_s = 10^3$, $W_s = 10^4$ at $t = 8000$. Other parameters: $G = 0.3$, Ma $= 0$, We $= 10$, $\beta = 0$, Bi $= 1$, and $L = 100$.

where h_0, $t_\nu = [\frac{\nu}{(g\sin\beta)^2}]^{1/3}$, and $l_\nu = (\frac{\nu^2}{g\sin\beta})^{1/3}$ are the mean thickness of the film, viscous-gravity time, and viscous-gravity length, respectively; $\nu = \mu/\rho$ is the kinetic viscosity of the fluid.

After rescaling the governing Eqs. 1(a)–1(c) and dropping all $*$ superscripts from the variables, we obtain the dimensionless governing equations

$$\nabla \cdot \boldsymbol{u} = 0, \tag{24a}$$

$$3\mathrm{Re}[\boldsymbol{u}_t + (\boldsymbol{u}\cdot\nabla)\boldsymbol{u}] = -\nabla p + \nabla^2\boldsymbol{u} + \frac{1}{\sin\beta}\boldsymbol{e}_g, \tag{24b}$$

$$3\mathrm{Pe}[T_t + (\boldsymbol{u}\cdot\nabla)T] = \nabla^2 T, \tag{24c}$$

where $\mathrm{Re} = \frac{gh_0^3\sin\beta}{3\nu^2}$ and $\mathrm{Pe} = \mathrm{RePr}$ are the Reynolds number and Peclét number with $\mathrm{Pr} = \nu/k$ (Prandtl number), respectively; $\boldsymbol{e}_g = (\sin\beta, -\cos\beta)$ represents the gravity direction.

The dimensionless boundary conditions on the substrate, $y = S(x,t)$, are

$$u = 0,\ v = S_t,\ T = 1, \tag{25a}$$

$$B_s S_t = W_s S_{xx} - (p - \cot\beta) - 2[S_x(u_y + v_x) - v_y], \tag{25b}$$

where $B_s = \frac{\rho_s h_s d_s h_0}{\mu}$ and $W_s = \frac{\sigma_s}{\rho g {h_0}^2 \sin\beta}$ are newly defined dimensionless damping and dimensionless tension coefficients, respectively. Here we consider the first-order model, and the terms of $O(S_x^2)$ with its higher order are neglected.

The dimensionless boundary conditions on the free interface, $y = H(x,t)$, become

$$u_y + v_x + 2H_x(v_y - u_x) = -\mathrm{Ma}T_x^i, \tag{25c}$$

$$-p - 2H_x(u_y + v_x) + 2v_y = \mathrm{We}\left(1 - \frac{\mathrm{Ma}}{\mathrm{We}}T^i\right)H_{xx}, \tag{25d}$$

$$H_x T_x - T_y = \mathrm{Bi}T, \tag{25e}$$

where $\mathrm{Ma} = \frac{\sigma_T(T_s - T_\infty)}{\rho g h_0^2 \sin\beta}$, $\mathrm{We} = \frac{\sigma_0}{\rho g h_0^2 \sin\beta}$, and $\mathrm{Bi} = \frac{h_g h_0}{\lambda}$ are newly defined Marangoni number, Weber number, and Biot number, respectively. The terms of $O(H_x^2)$ and higher are neglected. In this paper, we assume that surface tension is strong, and We $\gg$ Ma, such that the term $\frac{\mathrm{Ma}}{\mathrm{We}}T^i$ in Eq. (25d) could be neglected. The dimensionless kinematic condition on the free liquid surface remains unchanged as

$$v = H_t + uH_x. \tag{26}$$

Based on the long-wave assumption, the temporal and spatial variations of the interfacial slope are very slow, where we assume that $\partial_{t,x} \sim \epsilon \ll 1$. Therefore, we could make the following transformation:

$$(\partial_t, \partial_x) = \epsilon(\partial_{\tilde{t}}, \partial_{\tilde{x}}),\ \partial_{xx} = \epsilon^2\partial_{\tilde{x}\tilde{x}},\ v = \epsilon\tilde{v}. \tag{27}$$

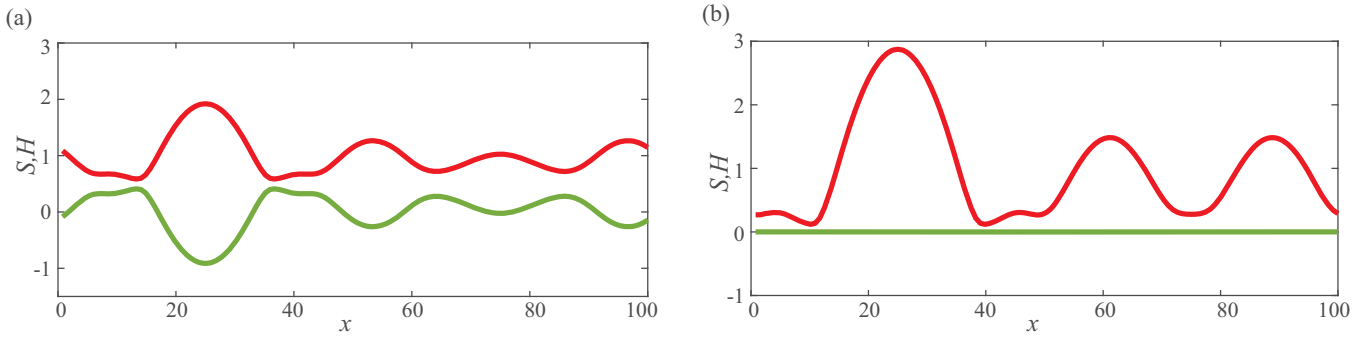

FIG. 9. The profiles of liquid film H [upper (red) line] and substrate S [lower (green) line] for (a) the case of a very compliant substrate with $B_s = 1, W_s = 10$ at $t = 1250$; (b) the case of a rigid substrate with $B_s = 10^3$, $W_s = 10^4$ at $t = 1700$. Other parameters: $G = 0$, Ma $= 2$, We $= 10$, $\beta = 0$, Bi $= 1$, and $L = 100$.

For simplicity, we drop the tildes in Eq. (27), and Eqs. (24a)–(24c) are restated as

$$u_x + v_y = 0, \tag{28a}$$

$$3\epsilon \mathrm{Re}(u_t + uu_x + vu_y) = -\epsilon p_x + \epsilon^2 u_{xx} + u_{yy} + 1, \tag{28b}$$

$$3\epsilon^2 \mathrm{Re}(v_t + uv_x + vv_y) = -p_y + \epsilon^3 v_{xx} + \epsilon v_{yy} - \cot\beta, \tag{28c}$$

$$3\epsilon \mathrm{Pe}(T_t + uT_x + vT_y) = \epsilon^2 T_{xx} + T_{yy}. \tag{28d}$$

The boundary conditions at $y = S(x,t)$ become

$$u = 0,\ v = S_t,\ T = 1, \tag{29a}$$

$$\epsilon B_s S_t = \epsilon^2 W_s S_{xx} - (p - \cot\beta) - 2\epsilon[S_x(u_y + \epsilon^2 v_x) - v_y]. \tag{29b}$$

The boundary conditions at $y = H(x,t)$ become

$$u_y + \epsilon^2 v_x - 2\epsilon^2 u_x H_x + 2\epsilon^2 v_y H_x = -\epsilon \mathrm{Ma} T_x^i, \tag{29c}$$

$$p = -2\epsilon H_x(u_y + \epsilon^2 v_x) + 2\epsilon v_y - \epsilon^2 \mathrm{We} H_{xx}, \tag{29d}$$

$$\epsilon^2 H_x T_x - T_y - \mathrm{Bi} T = 0. \tag{29e}$$

The kinematic condition on the free interface remains unchanged.

We assume that Reynolds number is small where $\mathrm{Re} \simeq 1$. In this section, to take the effects of surface tension, wall tension, wall damping, and Marangoni effect into account, we assume $\mathrm{We} = O(\epsilon^{-2})$, $B_s = O(\epsilon^{-1})$, $W_s = O(\epsilon^{-2})$, $\mathrm{Ma} = O(1)$, and $\mathrm{Bi} = O(1)$. To simplify, we assume $\mathrm{Pr} \simeq 1$ and neglect the thermal convection.

Based on these assumptions and only considering the first-order $O(\epsilon)$ dynamics, we further expand the variables $[u, v, p, T]$ in power series of ϵ asymptotically, given as

$$[u, v, p, T] = [u^{(0)}, v^{(0)}, p^{(0)}, T^{(0)}] + \epsilon[u^{(1)}, v^{(1)}, p^{(1)}, T^{(1)}] + O(\epsilon^2), \tag{30}$$

where $[u^{(0)}, v^{(0)}, p^{(0)}, T^{(0)}]$ and $[u^{(1)}, v^{(1)}, p^{(1)}, T^{(1)}]$ represent the leading-order and first-order solutions, respectively.

After solving the equations at $O(1)$, we obtain the leading-order velocity components, pressure, and temperature as follows:

$$u^{(0)} = -\frac{1}{2}(y^2 - S^2) + H(y - S), \tag{31a}$$

$$v^{(0)} = S_t - \frac{1}{2}(y - S)^2 H_x + (H - S)(y - S)S_x, \tag{31b}$$

$$p^{(0)} = -\cot\beta(y - H) - \epsilon^2 \mathrm{We} H_{xx}, \tag{31c}$$

$$T^{(0)} = 1 - \frac{\mathrm{Bi}(y - S)}{1 + \mathrm{Bi}(H - S)}, \tag{31d}$$

where the corresponding leading-order temperature distribution at the free interface $y = H(x,t)$ is given as

$$T^{i,(0)} = \frac{1}{1 + \mathrm{Bi}(H - S)}. \tag{31e}$$

The first-order $O(\epsilon)$ streamwise velocity and pressure field are solved, respectively, as

$$u^{(1)} = 3\mathrm{Re}\left[\frac{(y-S)^4}{24} - \frac{(H-S)^3(y-S)}{6}\right](H-S)(H-S)_x + \left[\frac{(y-S)^3}{6} - \frac{(H-S)(y-S)}{2}\right](H-S)_t\Bigg\} + \left[\left(\frac{1}{2}y^2 - Hy\right) - \left(\frac{1}{2}S^2 - HS\right)\right](\cot\beta H_x - \epsilon^2 \mathrm{We} H_{xxx}) + \frac{\mathrm{MaBi}(H-S)_x}{[1 + \mathrm{Bi}(H-S)]^2} y, \tag{32a}$$

$$p^{(1)} = -(y - H)H_x - 2(H - S)(H - S)_x. \tag{32b}$$

The detailed derivation of leading-order and first-order solutions are given in Appendix A.

Furthermore, after substituting $u = u^{(0)} + \epsilon u^{(1)}$ into the kinematic condition, which is written in the form of mass conservation as

$$(H - S)_t + \partial_x \int_S^H u^{(0)} + \epsilon u^{(1)} dy = 0, \tag{33}$$

we yield

$$(H - S)_t + (H - S)^2(H - S)_x + \epsilon\Bigg\{-\mathrm{Re}\left[-\frac{9(H-S)^6(H-S)_x}{40} - \frac{5(H-S)^4(H-S)_t}{8}\right] - \frac{(H-S)^3}{3}(\cot\beta H_x - \epsilon^2 \mathrm{We} H_{xxx}) + \frac{\mathrm{MaBi}(H-S)^2(H-S)_x}{2[1 + \mathrm{Bi}(H-S)]^2}\Bigg\}_x = 0. \tag{34}$$

To eliminate $(H - S)_t$ from the second term of $O(\epsilon)$ in Eq. (34), we introduce $(H - S)_t = -(H - S)^2(H - S)_x + O(\epsilon)$, and to simplify, we further define $\Lambda = H - S$ as the dimensionless thickness of the liquid film. We obtain the evolution equation describing the dynamics of the liquid film in the form

$$\Lambda_t + \Lambda^2 \Lambda_x + \epsilon\left[\frac{2\mathrm{Re}}{5}\Lambda^6 \Lambda_x + \frac{d^3}{3}(-\cot\beta H_x + \epsilon^2 \mathrm{We} H_{xxx}) + \frac{\mathrm{MaBi}}{2(1 + \mathrm{Bi}\Lambda)^2}\Lambda^2 \Lambda_x\right]_x = 0. \tag{35}$$

The evolution equation describing the dynamics of the compliant substrate is obtained by substituting $p|_{y=S} = p^{(0)}|_{y=S} + \epsilon p^{(1)}|_{y=S}$, $u^{(0)}|_{y=S}$, and $v^{(0)}|_{y=S}$ into (29b) as

$$\epsilon B_s S_t - \epsilon^2 W_s S_{xx} - \epsilon^2 \mathrm{We} H_{xx} + \cot\beta(\Lambda - 1) - \epsilon\Lambda(2S - H)_x = 0. \tag{36}$$

To eliminate ϵ, we further rescale Eqs. (35) and (36) via the following transformation:

$$\epsilon(\partial_t, \partial_x) \to (\partial_t, \partial_x). \tag{37}$$

We eventually yield

$$\Lambda_t + \Lambda^2\Lambda_x + \left[\frac{2\mathrm{Re}}{5}\Lambda^6\Lambda_x + \frac{\Lambda^3}{3}(-\cot\beta H_x + \mathrm{We}H_{xxx}) + \frac{\mathrm{MaBi}}{2(1+\mathrm{Bi}\Lambda)^2}\Lambda^2\Lambda_x\right]_x = 0, \tag{38a}$$

$$B_s S_t - W_s S_{xx} - \mathrm{We}H_{xx} + \cot\beta(\Lambda - 1) - \Lambda(2S - H)_x = 0. \tag{38b}$$

Therefore, we obtain a new set of evolution equations that also accounts for the fluid inertia (Re), which are the extensional Benney-type equations [14]. By setting $S = 0$, we could recover the Benney-type equation obtained by Joo *et al*., who studied the long-wave instabilities of heated falling films on solid substrates [59]. Furthermore, by setting $\mathrm{Ma} = 0$, we could also obtain the Benney-type equation derived by Matar *et al*., who explored the dynamics of isothermal falling films on flexible inclines [31]. In particular, when B_s and/or W_s becomes infinitely large, the compliant wall is also recovered as a rigid wall. In this section, we mainly focus on the effects of fluid inertia (Re) and heating effect (Ma) on the dynamics of the liquid film and the substrate, where the effects of wall damping (B_s) and wall tension coefficient (W_s) have been discussed in detail by Matar *et al*. [31] and Peng *et al*. [36]. Therefore, in most situations, we fix Biot number (Bi), Weber number (We), wall damping (B_s), and wall tension (W_s) as 1, 100, 10, and 100, respectively.

B. Linear stability analysis

Following Sec. III, we first study the linear stability properties via the standard linear stability analysis. Equations (38a) and (38b) admit the following trivial steady solution:

$$[\bar{\Lambda}, \bar{S}] = [1, 0], \tag{39}$$

which is perturbed with an infinitesimal disturbance $[\Lambda', S']$,

$$[\Lambda, S] = [\bar{\Lambda}, \bar{S}] + [\Lambda', S']. \tag{40}$$

After linearization, we obtain

$$\Lambda'_t + \Lambda'_x + \left[\frac{2\mathrm{Re}}{5}\Lambda'_x + \frac{1}{3}(-\cot\beta H'_x + \mathrm{We}H'_{xxx}) + \frac{\mathrm{MaBi}}{2(1+\mathrm{Bi})^2}\Lambda'_x\right]_x = 0, \tag{41a}$$

$$B_s S'_t - W_s S'_{xx} - \mathrm{We}H'_{xx} + \cot\beta\Lambda' - (2S' - H')_x = 0, \tag{41b}$$

where $H' = \Lambda' + S'$.

A normal mode expansion is applied and thus the disturbances Λ' and S' are expressed by

$$[\Lambda', S'] = [\hat{\Lambda}, \hat{S}]\exp(ikx + \omega t), \tag{42}$$

where $[\hat{\Lambda}, \hat{S}]$ are the Fourier amplitudes of the disturbances, and the linear wave speed is given as $c_L = -\omega_i/k$.

Finally, by substituting the disturbance Eq. (42) into the linearized Eqs. (41a) and (41b), we obtain the following eigenvalue problem:

$$\omega\begin{pmatrix}\hat{\Lambda}\\ \hat{S}\end{pmatrix} = \begin{pmatrix}\mathcal{L}_{11} & \mathcal{L}_{12}\\ \mathcal{L}_{21} & \mathcal{L}_{22}\end{pmatrix}\begin{pmatrix}\hat{\Lambda}\\ \hat{S}\end{pmatrix}, \tag{43a}$$

where

$$\mathcal{L}_{11} = -ik + \frac{2\mathrm{Re}}{5}k^2 - \frac{1}{3}(\cot\beta k^2 + \mathrm{We}k^4) + \frac{\mathrm{MaBi}}{2(1+\mathrm{Bi})^2}k^2, \tag{43b}$$

$$\mathcal{L}_{12} = -\frac{1}{3}(\cot\beta k^2 + \mathrm{We}k^4), \tag{43c}$$

$$\mathcal{L}_{21} = \frac{1}{B_s}(-\mathrm{We}k^2 - \cot\beta - ik), \tag{43d}$$

$$\mathcal{L}_{22} = \frac{1}{B_s}(-W_s k^2 - \mathrm{We}k^2 + ik). \tag{43e}$$

Therefore, we obtain the dispersion curves $\omega_r(k)$ which show the effects of Re and Ma on the linear stability, as illustrated in Figs. 10(a) and 10(b), respectively. We observe that both the maximum growth rate (ω_r) and the cutoff wave number (k_c) increase with increasing Re and Ma, indicating the destabilizing roles of fluid inertia and Marangoni effects [see Figs. 10(a) and 10(b)]. In addition, compared with the case of $\beta = 0$, as we increase the Re and Ma, we do not see an obvious mode shift, indicating that only one mode (in the scope of sinuous and varicose modes found in Sec. III) is present in the case of $\beta = \pi/2$ [see Figs. 10(a) and 10(b)].

To further illustrate the effects of fluid inertia and Marangoni stresses on the linear stability, we obtain the neutral stability curves in the k_c-Ma plane with $\mathrm{Re} = 0$, 0.2, 0.5, 1, and 2, as plotted in Fig. 11. We notice that when the value of Ma is very small ($\mathrm{Ma} < 1$), the unstable regimes expand significantly with increasing Re. However, as we

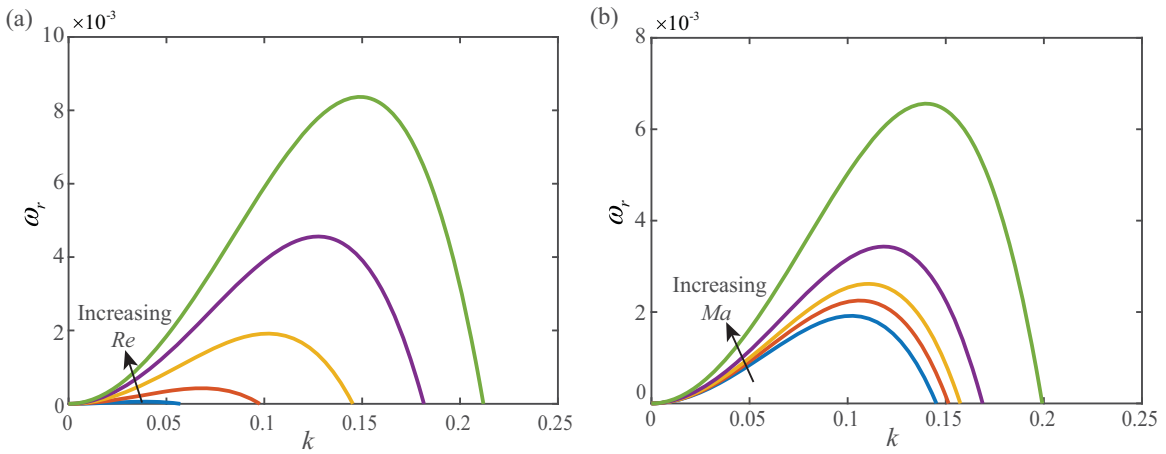

FIG. 10. The dispersion curves $\omega_r(k)$ showing the effects of (a) fluid inertia (Re = 0.2, 0.5, 1, 1.5, 2) without Marangoni stresses (Ma = 0); (b) Marangoni stresses (Ma = 0, 0.5, 1, 2, 5) with fluid inertia (Re = 1). Other parameters: We = 100, $B_s = 10$, $W_s = 100$, $\beta = \pi/2$, and Bi = 1.

further increase Ma into large values (Ma > 1), the unstable regions expand significantly with increasing Ma instead of Re. In all cases, k_c and the areas of unstable regions increase as Ma increases, further demonstrating the destabilizing effect of Marangoni stresses.

C. Steady traveling waves

Traveling waves, which propagate with a constant shape and downstream speed in a reference frame, are widely present in falling liquid films. These steady waves with finite amplitudes evolving from initial small disturbances are very crucial to understand the nonlinear dynamics of thin-film flows. Therefore, in this subsection, we explore the behavior of these steady traveling waves. First, we introduce the following transformation:

$$\xi = x - ct, \ \Lambda(x,t) = \Lambda(\xi),$$
$$H(x,t) = H(\xi), \ S(x,t) = S(\xi), \tag{44}$$

where c is the speed of the traveling waves. After substituting Eq. (44) into the evolution Eqs. (38a) and (38b), we eliminate the time dependence and obtain

$$-c\Lambda_\xi + \Lambda^2\Lambda_\xi + \left[\frac{2\mathrm{Re}}{5}\Lambda^6\Lambda_\xi + \frac{\Lambda^3}{3}(-\cot\beta H_\xi + \mathrm{We}H_{\xi\xi\xi}) + \frac{\mathrm{MaBi}}{2(1+\mathrm{Bi}\Lambda)^2}\Lambda^2\Lambda_\xi\right]_\xi = 0, \tag{45a}$$

$$-cB_sS_\xi - W_sS_{\xi\xi\xi} - \mathrm{We}H_{\xi\xi} + \cot\beta(\Lambda - 1) - \Lambda(2S - H)_\xi = 0, \tag{45b}$$

where $H = \Lambda + S$.

To fix the wave speed c, we impose a closed flow condition in the form

$$\frac{1}{L}\int_0^L (\Lambda + S)d\xi = 1, \tag{46}$$

where L is the length of computational domain.

Solutions of $\Lambda(\xi)$ and $S(\xi)$ are approximated via discrete Fourier series

$$\Lambda(\xi) = \sum_{-N/2}^{N/2} \hat{\Lambda}_n \exp(2in\pi\xi/L), \tag{47a}$$

$$S(\xi) = \sum_{-N/2}^{N/2} \hat{S}_n \exp(2in\pi\xi/L). \tag{47b}$$

where N is the Fourier mode and $\hat{\Lambda}_n$ and $\hat{S}_n$ are the Fourier coefficients. The resulting system is solved via Newton iterations which could converge rapidly to the solutions with a good initial guess. In addition, the numerical continuation technique is applied to track the solution branch as the change of parameter [57]. To start the continuation, a sinusoidal solution with a small amplitude and a nearly cutoff wave number k_c is applied, where k_c is obtained from the linear stability analysis. In this paper, we only consider the fast one-hump waves, because only the one-hump solution can be recognized during the evolution of the wave families, as theoretically demonstrated by Pumir *et al*. [60], and also such dominant wave structures are more likely to be observed experimentally.

However, we should notice that the presence of a strong nonlinear term, $\frac{2\mathrm{Re}}{5}\Lambda^6\Lambda_\xi$, due to inertia in Eq. (45a), will result in no stationary traveling-wave solutions when Re is beyond a critical value [5,60]. Therefore, to identify the validity domain of Eqs. (45a) and (45b), we also calculate the branches of the single-hump solitary wave solutions. A typical result showing the phase speed c as a function of Re with different Ma is plotted in Fig. 12. When Re is beyond the critical value Re^* (see the turning points in Fig. 12), two branches including a lower and an upper branches are present. In this situation, we could not obtain any stationary solitary wave solutions due to

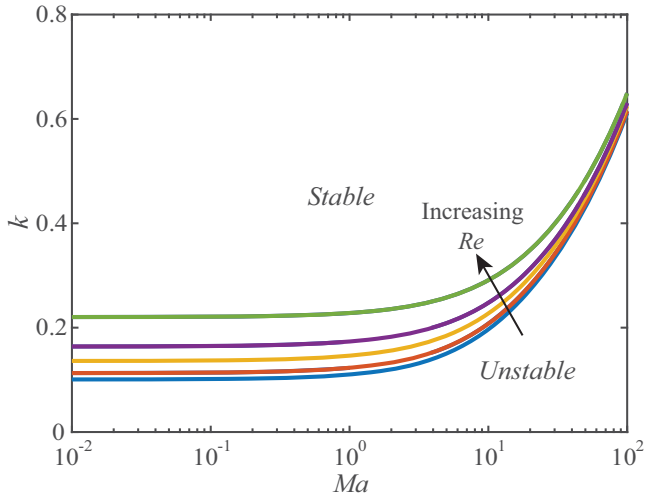

FIG. 11. Neutral stability curves in the parameter space spanned by Ma-k for $\mathrm{Re} = 0, 0.2, 0.5, 1, 2$. Other parameters: $\mathrm{We} = 100$, $B_s = 10$, $W_s = 100$, $\beta = \pi/2$, and $\mathrm{Bi} = 1$.

the unphysical finite-time blowup of solutions of Eq. (38a) [5]. In particular, we consider the case of a very rigid substrate, where $B_s = 10^4$ and $W_s = 10^5$, and adopt the identical values for other parameters ($\mathrm{Re} = 2.0667$, $\mathrm{We} = 874$, $\mathrm{Ma} = 0$, $\beta = \pi/2$, and $k = 0.011$) from the work of Kalliadasis *et al*. [5]. The calculated Re^* is 3.44 which is close to the value by Kalliadasis *et al*., where $\mathrm{Re}^* \simeq 3.5$ (see Ref. [5]), confirming the validity of our numerical technique.

A set of representative results showing the effects of fluid inertia on the traveling-wave profile of the liquid film, $H(\xi)$, as well as the deformation of the compliant substrate, $S(\xi)$, are shown in Fig. 13. We notice that increasing Re gives rise to a large amplitude of the traveling wave and a strong deformation of the substrate. In addition, the deformation of the fluid interface and the substrate are in the opposite direction, indicating that the varicose mode is present. The

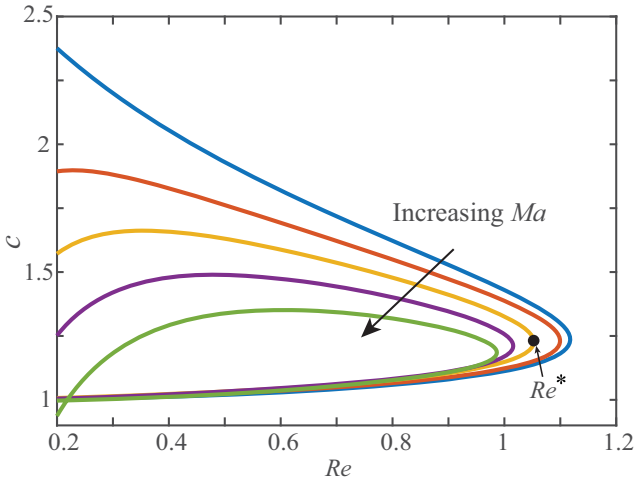

FIG. 12. The branches of single-hump solitary wave solutions for the phase speed c with $\mathrm{Ma} = 0, 1, 2, 3, 4$ and corresponding $k = 0.03, 0.06, 0.08, 0.10, 0.12$, respectively. Other parameters: $\mathrm{We} = 100$, $B_s = 10$, $W_s = 100$, $\beta = \pi/2$, $\mathrm{Bi} = 1$, and $L = 2\pi/k$.

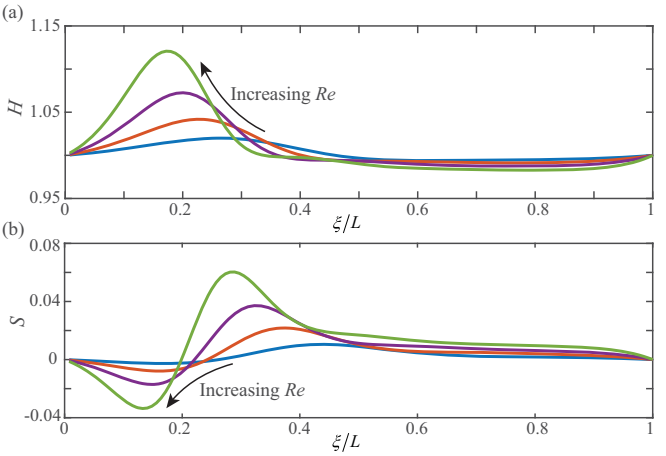

FIG. 13. Traveling-wave profiles showing the effects of fluid inertia ($\mathrm{Re} = 0.4, 0.6, 0.8, 1$) with $\mathrm{Ma} = 0$. Other parameters are $\mathrm{We} = 100$, $B_s = 10$, $W_s = 100$, $\beta = \pi/2$, $\mathrm{Bi} = 1$, $k = 0.05$, and $L = 40\pi$.

heating effects on $H(\xi)$ and $S(\xi)$ are illustrated in Fig. 14. The amplitudes of the traveling wave and wall deflection are larger in the case of liquid films with heating ($\mathrm{Ma} > 0$) compared with those without any heating ($\mathrm{Ma} = 0$), showing that Maragoni stresses accelerate squeezing the liquids between the free film interface and substrate. In addition, a stronger heating leads to a larger amplitude of the steady waves, as well as a more serious deflection of the flexible substrate compared with the cases of a weak heating. For instance, in the case of Fig. 14, compared with the case of $\mathrm{Ma} = 0.2$, liquid films with $\mathrm{Ma} = 1$ shows a 7.8% increase in the maximal hump height of the traveling waves and 60% increase in the maximal deformation of the compliant substrate, respectively. The enhancement of the Marangoni stresses on the instability of varicose mode is similar with the results for the case of a horizontal substrate with heating effects.

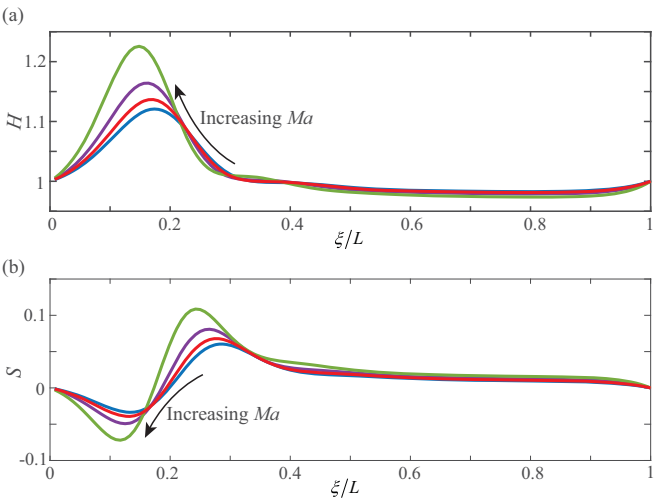

FIG. 14. Traveling-wave profiles showing the effects of Marangoni stresses ($\mathrm{Ma} = 0, 0.2, 0.5, 1$) with $\mathrm{Re} = 1$. Other parameters are $\mathrm{We} = 100$, $B_s = 10$, $W_s = 100$, $\beta = \pi/2$, $\mathrm{Bi} = 1$, $k = 0.05$, and $L = 40\pi$.

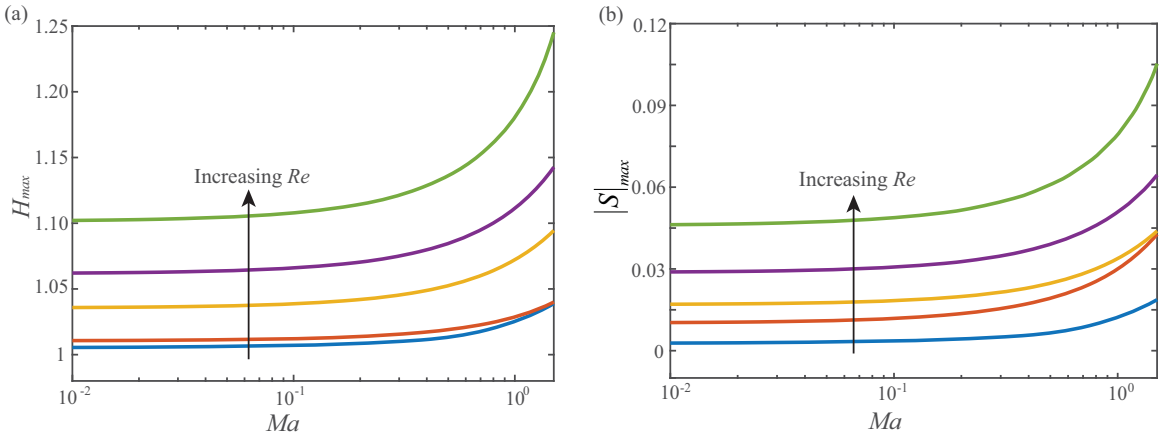

FIG. 15. The maximal wave height of the nonlinear wave $H_{\max}$ and the absolute value of the largest wall deflection $|S|_{\max}$ showing the Marangoni effect Ma with Re $= 0.2, 0.4, 0.6, 0.8, 1$. Other parameters are We $= 100$, $B_s = 10$, $W_s = 100$, Bi $= 1$, $\beta = \pi/2$, $k = 0.05$, and $L = 40\pi$.

However, we notice that the position of ξ which corresponds to the maximal deformation of substrate is not synchronous (i.e., out-of-phase) with that of liquid film, which is modified by the fluid gravity term $[\Lambda^2\Lambda_\xi$ in Eq. (45a)] and different from the case of $\beta = 0$. In addition, in all the cases for $\beta = \pi/2$, we do not see the sinuous mode, which could be observed in the case of $\beta = 0$. Actually, for the case of falling liquid films, because the gravity direction is parallel to the substrate, the component of gravitational force, that is vertically toward the compliant substrate, is absent. In our calculations, we do not observe obvious preceding capillary ripples with short wavelengths (see Figs. 13 and 14), which is due to the damping effect of small dimensionless wall tension (here $W_s = 100$) on the amplitude of these interfacial capillary ripples [36].

To have a clear view of how fluid inertia and wall heating affect the behavior of traveling waves and the deformation of compliant substrate, we plot the maximal hump height of the nonlinear traveling waves $H_{\max}$ and the largest absolute value of the wall deformation $|S|_{\max}$ as a function of Ma with various Re, as shown in Figs. 15(a) and 15(b), respectively. We observe that when the Ma is small, typically Ma < 0.5, the $H_{\max}$ and $|S|_{\max}$ are strongly affected by Re, indicating that the shear stresses strongly accelerate the instability in this regime. However, as we increase Ma into large values, typically Ma > 0.5, we find that the Marangoni stresses begin to dominate the instability, where $H_{\max}$ and $|S|_{\max}$ increase rapidly with increasing Ma, agreeing well with the predictions of linear stability analysis. The corresponding nonlinear wave speed c as a function of Ma with various Re is also obtained and plotted in Fig. 16. In agreement with the results of the maximal hump height, Re and Ma play destabilizing roles, where c is promoted by increasing Re and/or Ma. We also plot the dependence of linear wave speed c_L on Ma in the case of Re $= 1$, which is obtained from Eqs. (43a)–(43e), and find that the linear wave speed c_L is smaller than the nonlinear wave speed c (see dashed line in Fig. 16), further demonstrating that the calculated traveling waves belong to the faster one-hump wave.

D. Nonlinear simulations

To examine the fully nonlinear spatiotemporal dynamics, we must perform the time-dependent nonlinear simulations of the full evolution systems. Following Sec. III, we apply periodical boundary conditions in domain $x \in [0, L]$ and use the discrete Fourier series to approximate the spatial solutions of Eqs. (38a) and (38b) in the form of

$$\Lambda(x,t) = \sum_{-N/2}^{N/2} \hat{\Lambda}_n(t)\exp(2in\pi x/L), \tag{48a}$$

$$S(x,t) = \sum_{-N/2}^{N/2} \hat{S}_n(t)\exp(2in\pi x/L), \tag{48b}$$

where $\hat{\Lambda}_n(t)$ and $\hat{S}_n(t)$ are the Fourier coefficients and N is the number of Fourier mode.

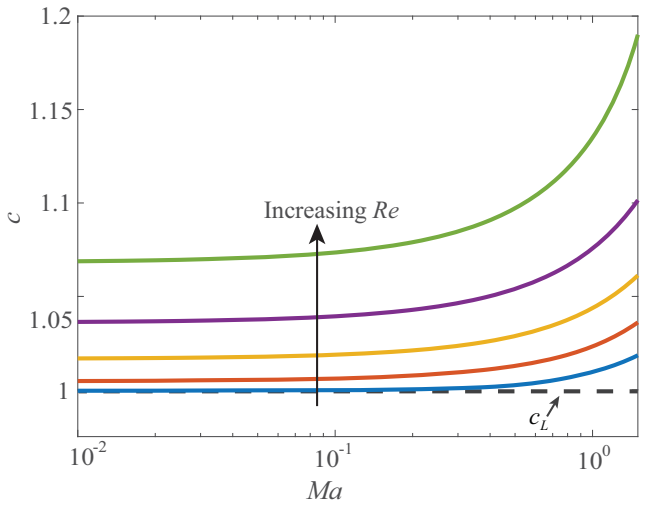

FIG. 16. The nonlinear wave speed c showing the Marangoni effect Ma with Re $= 0.2, 0.4, 0.6, 0.8, 1$. The linear wave speed c_L with Re $= 1$ is also plotted. Other parameters are We $= 100$, $B_s = 10$, $W_s = 100$, $\beta = \pi/2$, Bi $= 1$, $k = 0.05$, and $L = 40\pi$.

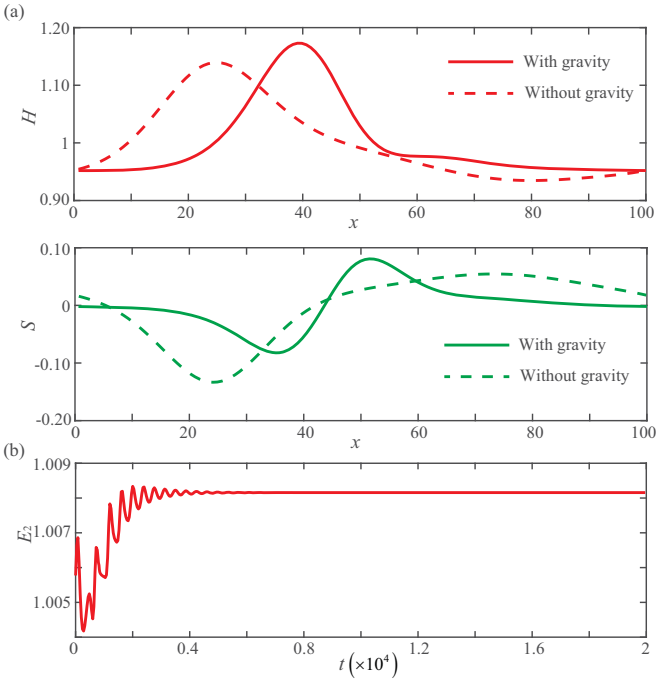

FIG. 17. (a) Typical time-dependent calculations showing the profiles of liquid film H and substrate S with the gravity term [by retaining $\Lambda^2\Lambda_x$ in Eq. (38a)] at $t = 3200$ (solid lines) and without the gravity term [by removing $\Lambda^2\Lambda_x$ in Eq. (38a)] at $t = 240$ (dashed lines). (b) The temporal evolution of the energy norm E_2 for the case with the gravity term in a large timescale, $t = 2 \times 10^4$. Other parameters are Re $= 1$, Ma $= 1$, We $= 100$, $B_s = 10$, $W_s = 100$, Bi $= 1$, $\beta = \pi/2$, and $L = 100$.

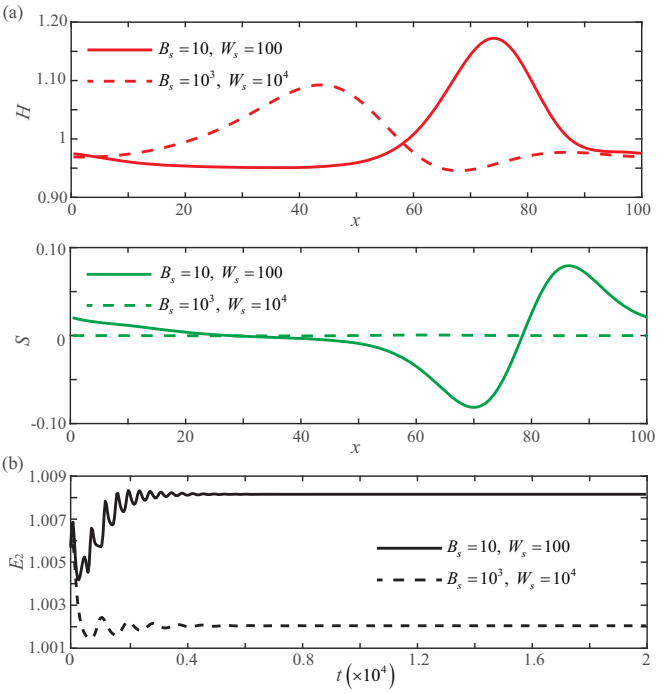

FIG. 18. (a) The profiles of liquid film H and substrate S for the case of a very compliant substrate with $B_s = 10, W_s = 100$ at $t = 2000$ (solid lines), and the case of a very rigid substrate with $B_s = 10^3$, $W_s = 10^4$ at $t = 2000$ (dashed lines); (b) the temporal evolution of the energy norm E_2 for both cases in a large timescale, $t = 2 \times 10^4$. Other parameters are Re $= 1$, Ma $= 1$, We $= 100$, Bi $= 1$, $\beta = \pi/2$, and $L = 100$.

Initially, when $t = 0$, we apply an initially harmonic perturbation to the liquid film and the compliant substrate remains flat, and thus

$$\Lambda(x, 0) = 1 + 0.1\sin(2\pi x/L), \tag{49a}$$

$$S(x, 0) = 0. \tag{49b}$$

Moreover, to measure the energy transfer from base flow into the disturbances, we also define an energy norm in the following form:

$$E_2 = \int_0^L \Lambda^2 dx. \tag{50}$$

We explore the spatiotemporal evolution of interface shapes of the liquid film and the compliant substrate in a computational domain ($L = 100$) with Re $=$ Ma $= 1$, as plotted in Fig. 17(a). We observe that, at $t = 2500$, the initially small amplitude sinusoidal wave in the form of Eq. (49a) evolves into waves with a relatively large hump ($H_{\max} \simeq 1.18$) and the initially flat substrate in the form of Eq. (49b) deforms with an amplitude of $|S| \simeq 0.08$. Consistently with the traveling-wave profiles, the deformation direction of the compliant substrate is opposite with that of liquid surface and the x positions corresponding to the peak of their largest deformations are not synchronous. Actually, the nonsynchronous deformations of the free liquid interface and substrate are induced by the fluid gravity [the term $\Lambda^2\Lambda_x$ in Eq. (38a)]. To confirm this argument, we also perform the time-dependent simulations of the modified Eqs. (38a) and (38b) without considering the term of $\Lambda^2\Lambda_x$. We find that, after removing the gravity term, the deformation of liquid interface and that of the substrate are in the opposite direction synchronously [see dashed lines in Fig. 17(a)], confirming that the out-of-phase behavior observed in the varicose mode is caused by the fluid gravity [see solid lines in Fig. 17(a)].

The temporal evolution of the energy norm E_2 for the case with the gravity term in a large timescale ($t = 2 \times 10^4$) is plotted in Fig. 17(b). We find that, at very early time, $t < 500$, the value of energy norm E_2 decreases with time. Afterward, $t > 500$, the value of energy norm E_2 gradually increases and then oscillates with time. However, after a very long time, $t > 6000$, the oscillation is damped and the value of energy norm E_2 levels off, indicating that the system eventually evolves into a saturated steady state with a constant energy norm [see Fig. 17(b)]. These results obtained via time-dependent simulations in the case of $\beta = \pi/2$ are consistent with the predications of linear stability analysis and the traveling-wave solutions. In addition, to have a more general understanding of our results, we also investigate the time-dependent profiles of the liquid film and substrate for the cases of compliant substrates with two different intermediate inclined angles ($\beta = \pi/3$ and $\beta = \pi/6$), which are presented in Appendix C.

Finally, consistent with Sec. III C, we also compare the time-dependent numerical results of a very compliant

substrate with those of a very solid substrate. As we increase the wall damping and wall tension coefficients from small values, where $B_s = 10$ and $W_s = 100$, into very large values, where $B_s = 10^3$ and $W_s = 10^4$, we could also find that the compliant substrate recovers as a rigid substrate [see Fig. 18(a)]. Due to the strong damping effect in the case of a rigid substrate, the deformation of the liquid-air interface is smaller than that of a very compliant substrate, indicating the system is more stable when the substrate is very rigid, which is further supported by the temporal evolution of energy norm (E_2) [see Fig. 18(b)].

V. CONCLUSIONS

In this paper, we study the dynamic behavior of thin-film flows over a uniformly heated, compliant substrate. Using long-wave approximation, a simplified membrane model, and Fourier's law, we derive a set of partial differential equations to describe the spatiotemporal evolution of the thin liquid films and the profile of the wall deflection with the consideration of thermocapillary effect. We consider two different cases, thin liquid films on a horizontally placed substrate ($\beta = 0$) and down a vertically placed substrate ($\beta = \pi/2$), respectively.

For $\beta = 0$, we derive a set of lubrication-type evolution equations without taking the fluid inertia into account, and two nondimensional numbers, gravity number G and Marangoni number Ma, are introduced to describe the fluid gravity and thermocapillary effect, respectively. To understand the effects of fluid gravity and wall heating, we perform linear stability analysis and time-dependent simulations of the fully nonlinear evolution equations. Two different modes, termed as sinuous mode where the liquid-air and liquid-substrate interfaces are in phase and varicose mode where two interfaces are in phase opposition, are identified, which are caused by fluid gravity (G) and Marangoni stresses (Ma), respectively. For $\beta = \pi/2$, we rederive a set of Benney-type long-wave equations with considering a weak fluid inertia (Re $\simeq 1$), and the effects of Re and Ma are also examined by the linear stability analysis and nonlinear dynamical simulations. In the case of $\beta = \pi/2$, because the gravity direction is parallel to the substrate, only the varicose mode caused by fluid inertia and Marangoni stresses is observed. However, the presence of the fluid gravity modifies the form of the varicose mode, making the deformations of two interfaces out of phase. In particular, for $\beta = \pi/2$, we also seek the nonlinear traveling-wave solutions, revealing that fluid inertia and/or Marangoni effect enhance the maximal hump height and phase speed of the traveling waves. In both cases, the introduction of a strong wall heating results in large deformations of both the liquid film and the compliant substrate.

In conclusion, our results extend the study on the dynamics of thin film flows over heated compliant substrates and thus enrich the understanding of the interaction between liquid flows and compliant materials in nonisothermal environments. Future work will focus on experimental verification of the results presented in this paper as well as on exploring the dynamics of thin-film flows down the heated compliant substrate in the scope of flows at moderate Reynolds numbers.

ACKNOWLEDGMENTS

We thank Professor Howard A. Stone for very helpful discussions. Y.C. acknowledges the support from the Hong Kong Ph.D. Fellowship Scheme (Grant No. PF14-15113) funded by the Research Grants Council (RGC) of Hong Kong. Z.D. acknowledges the warm hospitality of Professor R. Liu when visiting Gui Lin University of Electronic Technology. This work is partially supported by Guangxi Natural Science Foundation (Grant No. 2018GXNSFAA281331).

APPENDIX A: DERIVATION OF LEADING-ORDER AND FIRST-ORDER SOLUTIONS

In this work, we only consider the first order $O(\epsilon)$ dynamics, therefore, Eqs. (28a)–(28d) become

$$u_x + v_y = 0, \tag{A1a}$$

$$3\epsilon \mathrm{Re}(u_t + uu_x + vu_y) = -\epsilon p_x + u_{yy} + 1, \tag{A1b}$$

$$-p_y + \epsilon v_{yy} - \cot\beta = 0, \tag{A1c}$$

$$T_{yy} = 0. \tag{A1d}$$

The boundary conditions at $y = S(x,t)$, Eqs. (29a) and (29b), are reduced to

$$u = 0,\ v = S_t,\ T = 1, \tag{A2a}$$

$$\epsilon B_s S_t = \epsilon^2 W_s S_{xx} - (p - \cot\beta) - 2\epsilon(S_x u_y - v_y). \tag{A2b}$$

The boundary conditions at $y = H(x,t)$, Eqs. (29c)–(29e), are reduced to

$$u_y = -\epsilon \mathrm{Ma} T_x^i, \tag{A2c}$$

$$p = -2\epsilon H_x u_y + 2\epsilon v_y - \epsilon^2 \mathrm{We} H_{xx}, \tag{A2d}$$

$$T_y + \mathrm{Bi} T = 0. \tag{A2e}$$

The kinematic condition on the free interface remains unchanged, given as

$$v = H_t + uH_x. \tag{A3}$$

The variables $[u, v, p, T]$ is expanded in power series of ϵ as

$$[u, v, p, T] = [u^{(0)}, v^{(0)}, p^{(0)}, T^{(0)}] + \epsilon[u^{(1)}, v^{(1)}, p^{(1)}, T^{(1)}] + O(\epsilon^2). \tag{A4}$$

1. The leading-order solutions

We substitute Eq. (A4) into the governing Eqs. (A1a)–(A1d) and the boundary conditions, Eqs. (A2a)–(A2e), and obtain the leading-order governing equations, written as

$$u_x^{(0)} + v_y^{(0)} = 0, \quad u_{yy}^{(0)} = -1, \quad p_y^{(0)} = -\cot\beta, \quad T_{yy}^{(0)} = 0. \tag{A5}$$

The associated boundary conditions at $y = S(x,t)$ are written as

$$u^{(0)} = 0, \quad v^{(0)} = S_t, \quad T^{(0)} = 1. \tag{A6a}$$

The associated boundary conditions at $y = H(x,t)$ are written as

$$u_y^{(0)} = 0, \quad p^{(0)} = -\epsilon^2 \mathrm{We} H_{xx}, \quad T_y^{(0)} + \mathrm{Bi} T^{(0)} = 0. \tag{A6b}$$

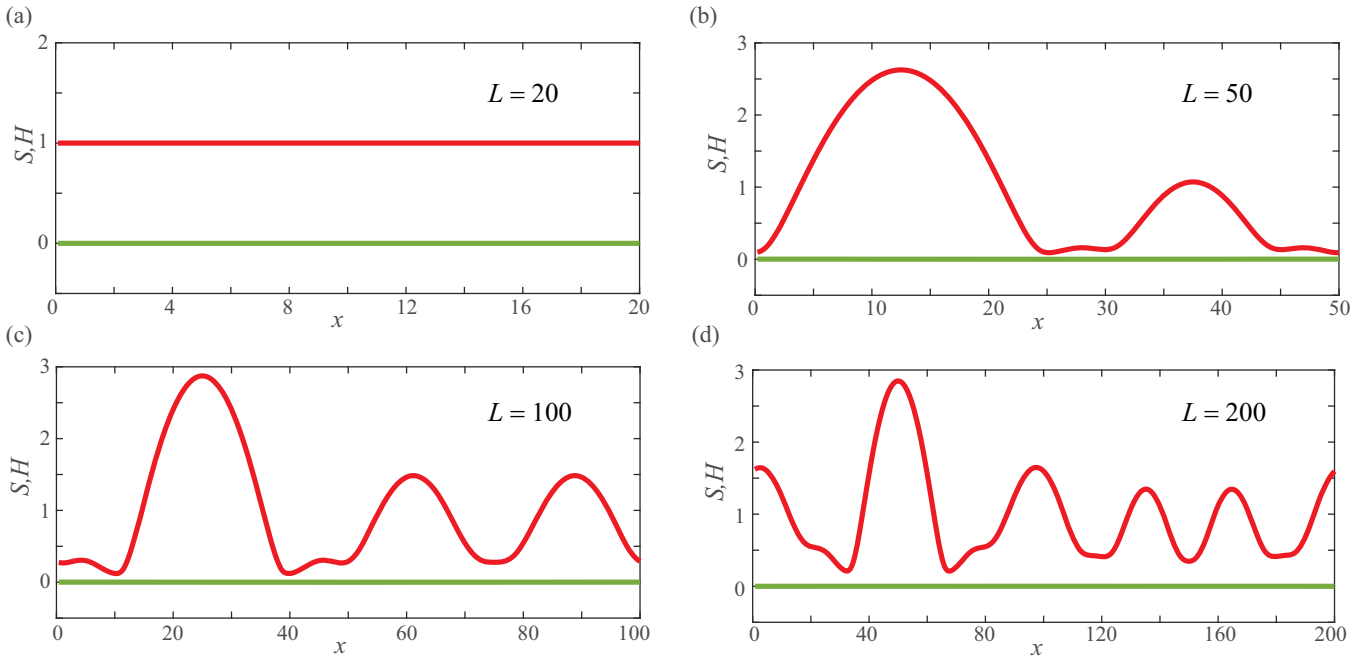

FIG. 19. The profiles of liquid film H [upper (red) lines] and substrate S [lower (green) lines] for various lengths of the computation domain (L): (a) $L = 20$ at $t = 1250$; (b) $L = 50$ at $t = 950$; (c) $L = 100$ at $t = 1700$; and (d) $L = 200$ at $t = 3900$. Other parameters: $G = 0$, Ma $= 2$, We $= 10$, $B_s = 10^3$, $W_s = 10^4$, $\beta = 0$, and Bi $= 1$.

Then, we obtain the leading-order velocity components, pressure, and temperature as follows:

$$u^{(0)} = -\frac{1}{2}(y^2 - S^2) + H(y - S), \tag{A7a}$$

$$v^{(0)} = S_t - \frac{1}{2}(y - S)^2 H_x + (H - S)(y - S)S_x, \tag{A7b}$$

$$p^{(0)} = -\cot\beta(y - H) - \epsilon^2 \mathrm{We} H_{xx}, \tag{A7c}$$

$$T^{(0)} = 1 - \frac{\mathrm{Bi}(y - S)}{1 + \mathrm{Bi}(H - S)}, \tag{A7d}$$

where the corresponding leading-order temperature distribution at the free interface $y = H$ is given as $T^{i,(0)} = \frac{1}{1+\mathrm{Bi}(H-S)}$.

2. The first-order solutions

Similarly, we could also extract the first-order governing equations, written as

$$\begin{aligned} &u_x^{(1)} + v_y^{(1)} = 0, \\ &u_{yy}^{(1)} = 3\mathrm{Re}\left(u_t^{(0)} + u^{(0)}u_x^{(0)} + v^{(0)}u_y^{(0)}\right) + p_x^{(0)}, \\ &p_y^{(1)} = v_{yy}^{(0)},\ T_{yy}^{(1)} = 0. \end{aligned} \tag{A8}$$

The associated boundary conditions at $y = S(x, t)$ are

$$u^{(1)} = 0, \quad v^{(1)} = S_t, \quad T^{(1)} = 0. \tag{A9a}$$

The associated boundary conditions at $y = H(x, t)$ are

$$\begin{aligned} &u_y^{(1)} = -\mathrm{Ma}T_x^{i,(0)}, \\ &p^{(1)} = -2H_x u_y^{(0)} + 2v_y^{(0)}, \\ &T_y^{(1)} + \mathrm{Bi}T^{(1)} = 0, \end{aligned} \tag{A9b}$$

$$p^{(1)} = -2H_x u_y^{(0)} + 2v_y^{(0)}, \tag{A9c}$$

$$T_y^{(1)} + \mathrm{Bi}T^{(1)} = 0. \tag{A9d}$$

Then the first-order streamwise velocity and pressure fields are solved, respectively, as

$$\begin{aligned} u^{(1)} = 3\mathrm{Re}\Bigg\{&\left[\frac{(y - S)^4}{24} - \frac{(H - S)^3(y - S)}{6}\right](H - S)(H - S)_x + \left[\frac{(y - S)^3}{6} - \frac{(H - S)(y - S)}{2}\right](H - S)_t\Bigg\} \\ &+ \left[\left(\frac{1}{2}y^2 - Hy\right) - \left(\frac{1}{2}S^2 - HS\right)\right](\cot\beta H_x - \epsilon^2 \mathrm{We} H_{xxx}) + \frac{\mathrm{MaBi}(H - S)_x}{[1 + \mathrm{Bi}(H - S)]^2}y, \end{aligned} \tag{A10a}$$

$$p^{(1)} = -(y - H)H_x - 2(H - S)(H - S)_x. \tag{A10b}$$

APPENDIX B: THE EFFECT OF COMPUTATIONAL LENGTH (L) FOR THE CASE OF A HORIZONTALLY RIGID SUBSTRATE

The length of computational domain (L) is assumed to have significant effects on the time-dependent numerical results of evolution Eqs. (14a) and (14b) [56]. To study the effects of computational length, following the numerical method in Sec. III C, we consider a rigid substrate where $B_s = 10^3$, $W_s = 10^4$ and set four different computational lengths where $L = 20, 50, 100, 200$, respectively. We observe that when $L = 20$, the initial perturbation in form of Eq. (22) is eventually damped and becomes flat, indicating that the thermocapillary waves with short wavelengths are suppressed (see Fig. 19), which is consistent with the predications of linear stability analysis.

APPENDIX C: TYPICAL RESULTS FOR THE CASES OF SUBSTRATE WITH INTERMEDIATE INCLINED ANGLES

In the main text, we only consider the cases of horizontal ($\beta = 0$) and vertical ($\beta = \pi/2$) substrates. To generalize our results, we further consider the cases of compliant substrates with two different intermediate inclined angles, where $\beta = \pi/3$ and $\beta = \pi/6$. Following the numerical method in Sec. IV D, we set $\beta = \pi/3$ and $\beta = \pi/6$, perform the time-dependent simulations of the Eqs. (38a) and (38b), and thus obtain the typical profiles of liquid-air and liquid-substrate interfaces, respectively, as shown in Fig. 20(a). In addition, we also plot the results for the case of a vertical substrate ($\beta = \pi/2$) into Fig. 20(b), showing that the deformations of the substrates for $\beta = \pi/3$ and $\beta = \pi/6$ are more serious than those of the case of $\beta = \pi/2$, which is due to the existence of vertical gravity component to the substrate in the cases of $\beta = \pi/3$ and $\beta = \pi/6$. In all cases, the profiles of liquid-air and liquid-substrate interfaces behave as the out-of-phase varicose mode because the parallel component of fluid gravity to the substrate is always present. The corresponding temporal evolutions of the energy norm E_2 for the three cases in a large timescale ($t = 2 \times 10^4$) are plotted in Fig. 20(b), showing that the amplitude of energy norm in the case of vertical substrate is larger than that of substrate with the intermediate inclined angle and the system is more unstable.

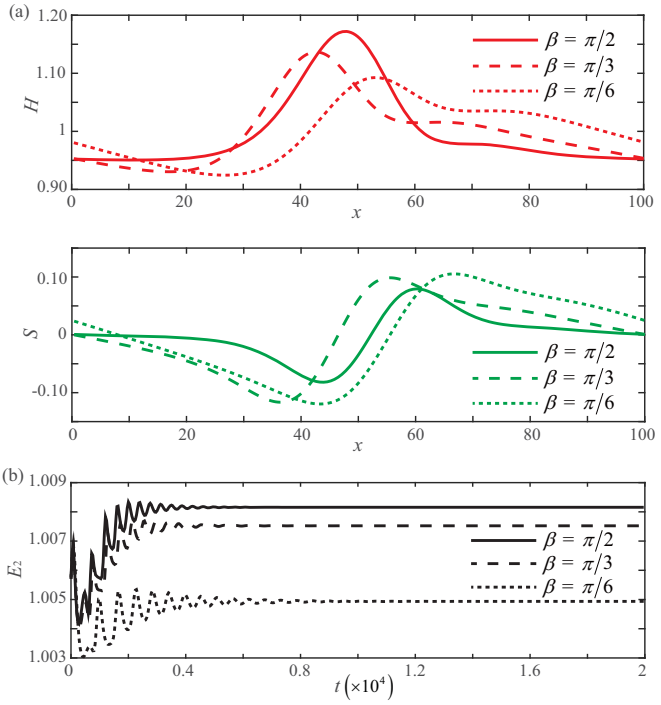

FIG. 20. (a) The profiles of liquid film H and substrate S with the inclined angles $\beta = \pi/2$ (solid lines), $\beta = \pi/3$ (dashed lines), and $\beta = \pi/6$ (dotted lines) at $t = 5000$. (b) The corresponding temporal evolution of the energy norm E_2 for $\beta = \pi/2$ (solid line), $\beta = \pi/3$ (dashed line), and $\beta = \pi/6$ (dotted line) in a large timescale, $t = 2 \times 10^4$. Other parameters are $\mathrm{Re} = 1$, $\mathrm{Ma} = 1$, $\mathrm{We} = 100$, $B_s = 10$, $W_s = 100$, $\mathrm{Bi} = 1$, and $L = 100$.

[1] S. J. Weinstein and K. J. Ruschak, Annu. Rev. Fluid Mech. **36**, 29 (2004).
[2] W. Shyy, M. Francois, H. Udaykumar, N. N'dri, and R. Tran-Son-Tay, App. Mech. Rev. **54**, 405 (2001).
[3] R. W. Griffiths, Annu. Rev. Fluid Mech. **32**, 477 (2000).
[4] H. E. Huppert, J. Fluid Mech. **554**, 299 (2006).
[5] S. Kalliadasis, C. Ruyer-Quil, B. Scheid, and M. G. Velarde, *Falling Liquid Films*, Vol. 176 (Springer Science & Business Media, Berlin, 2011).
[6] P. L. Kapitza and S. Kapitza, J. Exp. Theor. Phys. **19**, 105 (1949).
[7] G. F. Dietze, F. Al-Sibai, and R. Kneer, J. Fluid Mech. **637**, 73 (2009).
[8] E. A. Demekhin, E. N. Kalaidin, S. Kalliadasis, and S. Y. Vlaskin, Phys. Rev. E **82**, 036322 (2010).
[9] I. Adebayo, Z. Xie, Z. Che, and O. K. Matar, Phys. Rev. E **96**, 013118 (2017).
[10] C. Duprat, F. Giorgiutti-Dauphiné, D. Tseluiko, S. Saprykin, and S. Kalliadasis, Phys. Rev. Lett. **103**, 234501 (2009).
[11] A. Charogiannis, F. Denner, B. G. van Wachem, S. Kalliadasis, and C. N. Markides, Phys. Rev. Fluids **2**, 014002 (2017).
[12] O. Reynolds, Philos. Trans. R. Soc. Lond. **177**, 157 (1886).
[13] A. Oron, S. H. Davis, and S. G. Bankoff, Rev. Mod. Phys. **69**, 931 (1997).
[14] D. Benney, J. Math. Phys. **45**, 150 (1966).
[15] B. Gjevik, Phys. Fluids **13**, 1918 (1970).
[16] V. Y. Shkadov, Fluid Dyn. **2**, 29 (1967).
[17] Y. Y. Trifonov, J. Eng. Thermophys. **17**, 282 (2008).
[18] C. Ruyer-Quil and P. Manneville, Eur. Phys. J. B **15**, 357 (2000).
[19] C. Ruyer-Quil and P. Manneville, Phys. Fluids **14**, 170 (2002).
[20] J. Bico, É. Reyssat, and B. Roman, Annu. Rev. Fluid Mech. **50**, 629 (2018).
[21] A. Bunger and A. Cruden, J. Geophys. Res. **116**, B02203 (2011).
[22] C. Duprat, S. Protiere, A. Beebe, and H. Stone, Nature **482**, 510 (2012).
[23] E. R. Jerison, Y. Xu, L. A. Wilen, and E. R. Dufresne, Phys. Rev. Let. **106**, 186103 (2011).

[24] T. T. Al-Housseiny, I. C. Christov, and H. A. Stone, Phys. Rev. Let. **111**, 034502 (2013).
[25] J. Huang, M. Juszkiewicz, W. H. De Jeu, E. Cerda, T. Emrick, N. Menon, and T. P. Russell, Science **317**, 650 (2007).
[26] D. Kumar, J. D. Paulsen, T. P. Russell, and N. Menon, Science **359**, 775 (2018).
[27] D. Halpern and J. Grotberg, J. Fluid Mech. **244**, 615 (1992).
[28] D. Halpern and J. Grotberg, J. Biomech. Eng. **115**, 271 (1993).
[29] O. K. Matar and S. Kumar, SIAM J. Appl. Math. **64**, 2144 (2004).
[30] O. K. Matar and S. Kumar, J. Eng. Math. **57**, 145 (2007).
[31] O. K. Matar, R. V. Craster, and S. Kumar, Phys. Rev. E **76**, 056301 (2007).
[32] G. Sisoev, O. Matar, R. Craster, and S. Kumar, Chem. Eng. Sci. **65**, 950 (2010).
[33] P. Howell, J. Robinson, and H. Stone, J. Fluid Mech. **732**, 190 (2013).
[34] P. Howell, H. Kim, M. Popova, and H. Stone, J. Fluid Mech. **796**, 285 (2016).
[35] Z. Zheng, I. M. Griffiths, and H. A. Stone, J. Fluid Mech. **784**, 443 (2015).
[36] J. Peng, Y.-J. Zhang, and W.-L. Zhuge, J. Non-Newton. Fluid Mech. **210**, 85 (2014).
[37] L. Scriven and C. Sternling, J. Fluid Mech. **19**, 321 (1964).
[38] K. Smith, J. Fluid Mech. **24**, 401 (1966).
[39] S. Sreenivasan and S. Lin, Int. J. Heat Mass Transfer **21**, 1517 (1978).
[40] O. A. Kabov, B. Scheid, I. A. Sharina, and J.-C. Legros, Int. J. Therm. Sci. **41**, 664 (2002).
[41] P. M. Trevelyan, S. Kalliadasis, J. H. Merkin, and S. K. Scott, Phys. Fluids **14**, 2402 (2002).
[42] Z. Ding and T. N. Wong, Int. J. Heat Mass Transfer **90**, 689 (2015).
[43] M. C. Dallaston, D. Tseluiko, and S. Kalliadasis, Phys. Rev. Fluids **1**, 073903 (2016).
[44] Y. Chao, Z. Ding, and R. Liu, Chem. Eng. Sci. **175**, 354 (2018).
[45] R. Sarma and P. K. Mondal, Phys. Rev. E **97**, 043105 (2018).
[46] C. Ruyer-Quil, B. Scheid, S. Kalliadasis, M. G. Velarde, and R. K. Zeytounian, J. Fluid Mech. **538**, 199 (2005).
[47] B. Scheid, C. Ruyer-Quil, S. Kalliadasis, M. G. Velarde, and R. K. Zeytounian, J. Fluid Mech. **538**, 223 (2005).
[48] S. Saprykin, P. M. J. Trevelyan, R. J. Koopmans, and S. Kalliadasis, Phys. Rev. E **75**, 026306 (2007).
[49] S. Yang, K. Khare, and P.-C. Lin, Adv. Funct. Mater. **20**, 2550 (2010).
[50] M. Kobayashi, W. Zavadoski, W. Kalriess, I. Smith, and S. Kishida, U.S. Patent No. 6,887,494 (2005). Washington, DC: U.S. Patent and Trademark Office.
[51] C. A. Dragon and J. B. Grotberg, J. Fluid Mech. **231**, 135 (1991).
[52] H. Atabek and H. Lew, Biophy. J. **6**, 481 (1966).
[53] A. E. Hosoi and L. Mahadevan, Phys. Rev. Let. **93**, 137802 (2004).
[54] Z.-Q. Zhou, J. Peng, Y.-J. Zhang, and W.-L. Zhuge, J. Fluid Mech. **802**, 583 (2016).
[55] G. Gittens, J. Colloid Interface Sci. **30**, 406 (1969).
[56] A. Oron, Phys. Fluids **12**, 1633 (2000).
[57] Z. Ding, J. Xie, T. N. Wong, and R. Liu, J. Fluid Mech. **752**, 66 (2014).
[58] A. Cazabat, F. Heslot, S. Troian, and P. Carles, Nature **346**, 824 (1990).
[59] S. Joo, S. Davis, and S. Bankoff, J. Fluid Mech. **230**, 117 (1991).
[60] A. Pumir, P. Manneville, and Y. Pomeau, J. Fluid Mech. **135**, 27 (1983).